Mathematical Biosciences and Engineering

https://www.aimspress.com/journal/mbe

MBE, 22(12): 3262–3294.
DOI: 10.3934/mbe.2025120
Received: 12 September 2025
Revised: 05 October 2025
Accepted: 30 October 2025
Published: 11 November 2025

Research article

Emerging infectious disease dynamics with compliance and isolation resource constraints

Xinru Li, Ning Wang and Shengqiang Liu*

School of Mathematical Sciences, Tiangong University, Tianjin 300387, China

* **Correspondence:** Email: sqliu@tiangong.edu.cn.

Abstract: The effectiveness of isolation strategies against emerging infectious diseases (EIDs) is critically undermined by two interacting factors: Limited resource capacity and imperfect public compliance, yet their combined impact remains poorly quantified. We develop an ordinary differential equation (ODE) model incorporating a saturation function for resource limits and a compliance parameter (ϵ) to quantify their nonlinear interaction. Theoretical analysis reveals a resource-driven backward bifurcation, indicating that reducing a basic reproduction number R_0 below 1 is necessary but may be insufficient for disease elimination when isolation capacity is critically low. Numerically, we identify a counterintuitive paradox: High compliance amplifies the infection risk when isolation resources are severely constrained. The simulation results classify the dynamic regimes under various parameter settings and reveal the qualitative impact of different isolation strategies. The study finds that increasing isolation resources, combined with a certain level of compliance, significantly reduces the infection risk and aids in disease control. Notably, specific transmission patterns emerge when isolation resources are inadequate, resulting in elevated infection risks even when compliance is high. Our results underscore the imperative of synchronizing resource allocation with behavioral interventions, particularly during early outbreak stages, providing a framework for precision public health strategies.

Keywords: emerging infectious disease; dynamical model; constrained isolation resources; bifurcation; basic reproductive number

1. Introduction

Infectious diseases remain a major global health burden, causing over 15 million deaths annually—more than a quarter of global mortality [1]. Emerging infectious diseases (EIDs), defined as infections newly appearing or rapidly increasing in incidence or geographic range [1], include dengue fever, Influenza A (H1N1), Crimean-Congo hemorrhagic fever (CCHF), acute hepatitis in children, atypical pneumonia (SARS), and COVID-19. Such EIDs not only threaten public health but

also impose significant economic burdens worldwide [2–5], underscoring the critical need to study their disease transmission dynamics for guiding effective intervention strategies [6–8].

Globally, public health responses to EIDs commonly feature isolation, quarantine, contact tracing, and vaccination [9–14]. Isolation remains a cornerstone strategy that reduces contact rates and interrupts transmission pathways, playing a pivotal role in epidemic control [7, 15–19]. However, sudden outbreaks often strain existing healthcare systems, leading to insufficient isolation capacity that undermines containment efforts [20]. The COVID-19 pandemic starkly revealed the consistent limitation of isolation resources globally. For instance, the Chinese Center for Disease Control and Prevention (CDC) reported severe shortages [21], and New Zealand faced a critical gap with only approximately 6,000 isolation rooms available over an eight-week period [22]. Similar shortages were observed in South Korea, Italy, Spain, and Iran [23], demonstrating that limited isolation resources are a widespread global challenge. This study therefore first investigates how inadequate isolation resource capacity shapes an epidemic's dynamics and control.

The effectiveness of isolation also heavily depends on individual compliance. Factors such as household co-infection, mild or asymptomatic infections, and limited information accessibility decrease compliance with isolation protocols [24]. Even with legal enforcement or financial incentives, noncompliance persists [25, 26]. For instance, Steens et al. [27] documented age-related variations in isolation compliance, highlighting significant demographic heterogeneity. Addressing the impact of isolation compliance on an epidemic's transmission constitutes the second key focus of this work.

In practice, limited isolation resources and low public compliance often coexist, creating a synergistic limitation on disease control for which the combined impact remains poorly quantified. However, these studies often treat resource constraints and behavioral compliance in isolation. The coupled effects of these factors, particularly their nonlinear interaction leading to emergent dynamics like backward bifurcation, lack theoretical quantification. This gap motivates our systematic investigation into how these factors jointly influence transmission of infectious diseases and the design of effective interventions.

Mathematical modeling serves as a fundamental framework for analyzing infectious disease dynamics, offering critical insights since the seminal work of Kermack and McKendrick [28, 29]. It provides a quantitative tool to analyze an epidemic's transmission behavior, evaluate intervention strategies, and reveal counterintuitive dynamics that are difficult to discern through empirical methods alone. Recent studies have incorporated limited isolation capacity into compartmental models to better represent real-world constraints [30–33]. Ahmad and Seno [30] pioneered a Filippov-type susceptible-infectious-recovered-quarantined (SIRQ) model with piecewise smooth isolation capacity constraints, while Fu and Seno [31] extended this via delay-differential equations in their susceptible-infectious-recovered-infectious-quarantined (SIRIQ) framework to capture temporal resource allocation effects, which are approaches that neglect behavioral heterogeneity. In contrast to their model, which does not account for isolation compliance, we incorporate a compliance parameter to reveal the rich dynamics arising from the coupling of resource limitations and behavioral responses. Similarly, Wang et al. [23] used dynamic data-driven models to show that increasing healthcare resources and intensity of intervention effectively mitigated the spread of and deaths from COVID-19. In contrast, they independently calibrated resources and compliance, whereas we quantify the resource-behavior coordination threshold. Optimal control approaches have also been

developed that address limited isolation capacity, such as the strategy to balance epidemic control and resource costs proposed by Nenchev [34].

Behavioral compliance significantly affects the effectiveness of isolation. While Gao et al. [26] developed an ordinary differential equation (ODE) model to assess the combined effect of testing and isolation compliance, our study focuses specifically on quantifying the nonlinear interaction between isolation resource constraints (characterized by a saturation function) and isolation compliance. Statistical studies, such as the multivariate analysis of Foroozanfar et al. [24], have linked high compliance to outbreak containment, focusing on behavioral factors in conjunction with resource constraints.

To investigate the influence of these two factors on disease spread patterns, we construct an infectious disease model that simultaneously incorporates limited isolation capacity and imperfect compliance. Consequently, we represent resource limitations by a saturated isolation rate function and behavioral responses by a compliance parameter ϵ. We then derive the global dynamics associated with the basic reproduction number R_0 and analyze how it governs the behavior of the system. By classifying the dynamic regimes of the model and using numerical simulations in two subcases, we evaluate various intervention strategies.

Unlike Wang et al. [23], who empirically identified key factors through cross-country data comparisons, our theoretical approach focuses on intrinsic dynamics. Specifically, we employ numerical bifurcation analysis to reveal how parameters govern transitions between equilibrium states. This enables us to quantify resource-dependent tipping points—a critical advance for precision control.

To bridge this gap, we develop a unified ODE framework that simultaneously incorporates (i) saturation effects of finite isolation resources, (ii) time-varying compliance, and (iii) their synergistic impact on epidemic thresholds. This approach rigorously characterizes backward bifurcation as an emergent property of resource–behavior coupling (Theorem 3.4) and derives operational thresholds for resource allocation (Section 4.2).

The paper is organized as follows: Section 2 introduces the compartmental model with saturated isolation rates and compliance parameters. Section 3 presents the main theoretical results including the threshold dynamics and a bifurcation analysis. Section 4 provides numerical simulations exploring the parameter effects and isolation delays. Section 5 concludes with a discussion and future directions.

2. Model formulation

We develop a deterministic model to analyze the influence of isolation on the disease spread trends. The population is divided into five compartments: Susceptible individuals (S), infected individuals awaiting test results (I_T), untested or nonisolated infected individuals (I), isolated infected individuals (L_I), and recovered individuals (R).

Referring to [26], we assume that all newborns and individuals entering the population are susceptible, and they enter the susceptible compartment S at a recruitment rate of Λ. A proportion σ of new infections are tested, and infected individuals awaiting test results leave the compartment I_T at a rate θ. Among them, a proportion ϵ fail to isolate themselves and transition to the compartment I, while the remaining individuals move to the isolation compartment L_I at a rate of $(1-\epsilon)\theta$. The initial conditions are $S(0) > 0$, $I_T(0) > 0$, $I(0) > 0$, $L_I(0) > 0$, $R(0) > 0$, and the total population is given by

$N(t) = S(t) + I_T(t) + I(t) + L_I(t) + R(t)$. All other parameters are assumed to be non-negative. The parameters of the model are shown in Table 1. Our model is based on the following assumptions.

- In our formulation, the L_I compartment represents perfect isolation with no secondary infections, and individuals in the I_T compartment are less infectious while awaiting test results compared with those in the I compartment. Specifically, they are less infectious with a probability ρ. Therefore, the infection rate is given by:

$$\lambda(t) = \frac{\beta(\rho I_T(t) + I(t))}{N(t) - L_I(t)}.$$

- We assume perfect testing (no false positives or negatives). This assumption allows us to focus specifically on the interplay between resource constraints and compliance behavior. In reality, false negatives would increase the pool of unisolated infectious individuals, potentially exacerbating transmission. We incorporate a saturated isolation rate, inspired by [35], which takes the form $(1 - \epsilon)\theta I_T(t)/(1 + \delta I_T(t))$. Here, δ is a positive constant that quantifies the limitation level of isolation resources.

Table 1. Descriptions and values of parameters involved in the model (2.1).

Parameter	Description	Value	Units	Reference
Λ	Recruitment rate (new individuals entering the population)	1762	persons day^{-1}	[36]
β	Transmission rate of infected individuals	0.25	day^{-1}	Assumed
σ	Proportion of infections that are tested	0.85	–	[26]
ϵ	Proportion of infected individuals not isolated	0.1, 0.3, 0.5	–	[26]
$1 - \epsilon$	Compliance rate for isolation	0.9, 0.7, 0.5	–	[26]
θ	Rate of leaving the test result waiting period (inverse of average waiting time)	0.333	day^{-1}	[26]
γ_I	Recovery rate of nonisolated infected individuals	0.12	day^{-1}	Estimated from [26]
ρ	Reduction factor of infectiousness due to testing/isolation	0.7	–	Estimated from [26]
δ	Isolation resource efficiency parameter	0.0001–0.01	persons^{-1}	[37]
μ	Natural death rate	0.0107	year^{-1}	[36]
μ_I	Mortality rate of nonisolated infected individuals	–	day^{-1}	–
μ_{L_I}	Mortality rate of isolated infected individuals	–	day^{-1}	–
γ_{L_I}	Recovery rate of isolated infected individuals	–	day^{-1}	–

Motivated by Gao et al. [26], and based on our assumptions, we derive a general model (2.1) that

incorporates saturated isolation rates.

$$\begin{aligned}
\frac{\mathrm{d}S}{\mathrm{d}t} &= \Lambda - \lambda(t)S(t) - \mu S(t),\\
\frac{\mathrm{d}I_T}{\mathrm{d}t} &= \sigma\lambda(t)S(t) - (\mu+\mu_I)I_T(t) - \epsilon\theta I_T(t) - \frac{(1-\epsilon)\theta I_T(t)}{1+\delta I_T(t)},\\
\frac{\mathrm{d}I}{\mathrm{d}t} &= (1-\sigma)\lambda(t)S(t) + \epsilon\theta I_T(t) - (\mu+\mu_I+\gamma_I)I(t),\\
\frac{\mathrm{d}L_I}{\mathrm{d}t} &= \frac{(1-\epsilon)\theta I_T(t)}{1+\delta I_T(t)} - (\mu+\mu_{L_I}+\gamma_{L_I})L_I(t),\\
\frac{\mathrm{d}R}{\mathrm{d}t} &= \gamma_I I(t) + \gamma_{L_I}L_I(t) - \mu R(t),
\end{aligned} \tag{2.1}$$

where $\lambda(t) = \beta(\rho I_T(t) + I(t))/(N(t) - L_I(t))$.

The model is described by a system of ODEs as follows, and the corresponding flowchart is shown in Figure 1.

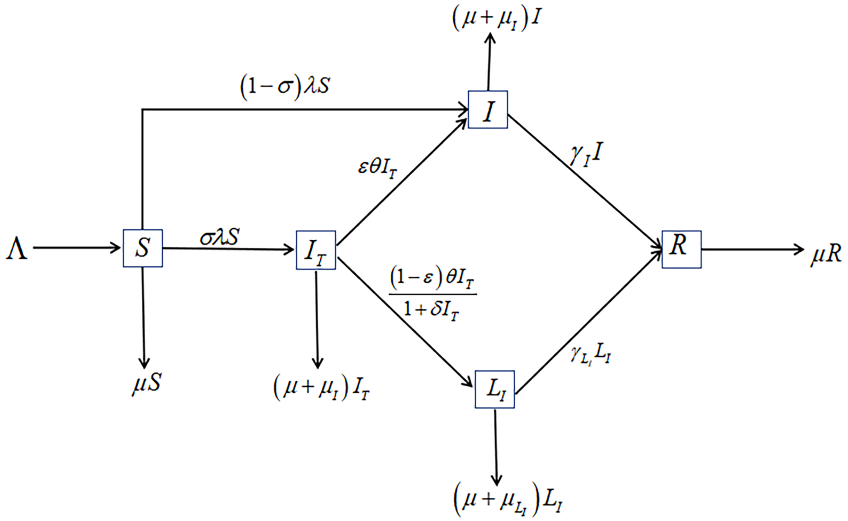

Figure 1. The schematic diagram of Model (2.1), which captures limited isolation capacity and isolation compliance.

To justify further simplification, we first analyze the total population dynamics. Summing all equations in Model (2.1) gives

$$\frac{\mathrm{d}N(t)}{\mathrm{d}t} = \Lambda - \mu N(t) - \mu_I I(t) - \mu_{L_I}L_I(t) - \mu_I I_T(t).$$

According to reports from the Tianjin CDC [38] and the Chinese CDC [21], the disease-induced mortality is less than 0.1%. The parameter sensitivity analysis of the basic reproduction number in Model (2.1) is presented in the Supplementary materials. Consequently, we set $\mu_I = 0$ and $\mu_{L_I} = 0$, leading to

$$\frac{\mathrm{d}N(t)}{\mathrm{d}t} = \Lambda - \mu N(t), \quad \text{with} \quad \lim_{t\to\infty} N(t) = \frac{\Lambda}{\mu}.$$

Furthermore, since World Health Organization (WHO) data [37] indicates that the number of isolated individuals is negligible compared with the total population, the infection force can be approximated

as $\lambda(t) = \beta(\rho I_T(t) + I(t))/N(t)$. Under the assumption of a constant total population $N = \Lambda/\mu$ at a steady state, the infection force simplifies to $\lambda(t) = \mu\beta(\rho I_T(t) + I(t))/\Lambda$.

With the abovementioned simplifications, we reduce Model (2.1) to the following system:

$$\begin{aligned}
\frac{\mathrm{d}S}{\mathrm{d}t} &= \Lambda - \lambda(t)S(t) - \mu S(t),\\
\frac{\mathrm{d}I_T}{\mathrm{d}t} &= \sigma\lambda(t)S(t) - \mu I_T(t) - \epsilon\theta I_T(t) - \frac{(1-\epsilon)\theta I_T(t)}{1+\delta I_T(t)},\\
\frac{\mathrm{d}I}{\mathrm{d}t} &= (1-\sigma)\lambda(t)S(t) + \epsilon\theta I_T(t) - (\mu+\gamma_I)I(t),\\
\frac{\mathrm{d}L_I}{\mathrm{d}t} &= \frac{(1-\epsilon)\theta I_T(t)}{1+\delta I_T(t)} - (\mu+\gamma_{L_I})L_I(t),\\
\frac{\mathrm{d}R}{\mathrm{d}t} &= \gamma_I I(t) + \gamma_{L_I} L_I(t) - \mu R(t),
\end{aligned} \tag{2.2}$$

where $\lambda(t) = \mu\beta(\rho I_T(t) + I(t))/\Lambda$.

Since the L_I and R compartments decouple from the rest, we focus on the following reduced three-dimensional system for subsequent analysis:

$$\begin{aligned}
\frac{\mathrm{d}S}{\mathrm{d}t} &= \Lambda - \lambda(t)S(t) - \mu S(t),\\
\frac{\mathrm{d}I_T}{\mathrm{d}t} &= \sigma\lambda(t)S(t) - \mu I_T(t) - \epsilon\theta I_T(t) - \frac{(1-\epsilon)\theta I_T(t)}{1+\delta I_T(t)},\\
\frac{\mathrm{d}I}{\mathrm{d}t} &= (1-\sigma)\lambda(t)S(t) + \epsilon\theta I_T(t) - (\mu+\gamma_I)I(t),
\end{aligned} \tag{2.3}$$

with $\lambda(t) = \mu\beta(\rho I_T(t) + I(t))/\Lambda$.

3. Model analysis

A comprehensive theoretical investigation is carried out in this section for Model (2.3), which incorporates saturated isolation rates. First, we demonstrate that all state variables remain non-negative and bounded for non-negative initial conditions, indicating that Model (2.3) is mathematically well-posed (Theorem 3.1). Subsequently, by employing the next-generation matrix (NGM) method, we derive the basic reproduction number R_0 and examine the local stability of the disease-free equilibrium (DFE) (Theorems 3.2 and 3.3). The existence of endemic equilibrium (EE) is further explored, and criteria for the emergence of backward bifurcation are derived (Theorem 3.4). In addition, we prove the uniform persistence of the disease (Theorem 3.6). Finally, we explore how changes in R_0 affect the qualitative behavior of the system, thereby offering a comprehensive characterization of the disease dynamics.

3.1. Well-posedness of the solutions

From a biological standpoint, the population variables should remain non-negative and bounded at all times. In this subsection, we prove the positivity and boundedness of the solutions of Model (2.3), thereby establishing the well-posedness of Model (2.3).

Theorem 3.1. *Model (2.3) admits a unique, bounded solution for all $t \geq 0$, given initial conditions within the domain*

$$D = \left\{(S, I_T, I) \in \mathbb{R}^3_+ \;\middle|\; S + I_T + I \leq \frac{\Lambda}{\mu}\right\}.$$

Furthermore, the compact set D is positively invariant under the flow of Model (2.3).

Proof. **Positivity:** Integrating the first equation of Model (2.3) yields

$$S(t) = e^{\int_0^t \left[\frac{\mu\beta}{\Lambda}\left(\rho I_T(x)+I(x)\right)-\mu\right]\mathrm{d}x}\left(S_0 + \int_0^t \lambda\, e^{-\int_0^s \left[\frac{\mu\beta}{\Lambda}\left(\rho I_T(x)+I(x)\right)-\mu\right]\mathrm{d}x}\,\mathrm{d}s\right) > 0.$$

Thus, $S(t) > 0$ for all $t \geq 0$. For the second equation, after suitable estimation, we have

$$\frac{\mathrm{d}I_T}{\mathrm{d}t} = \sigma\lambda(t)S(t) - \mu I_T - \epsilon\theta I_T - \frac{(1-\epsilon)\theta I_T}{1+\delta I_T} \quad \geq \quad \sigma\lambda(t)S(t) - \mu I_T - \epsilon\theta I_T - (1-\epsilon)\theta I_T.$$

Consequently

$$I_T(t) \geq e^{\int_0^t \left[\frac{\sigma\mu\beta\rho S(x)}{\Lambda}-\mu-\theta\right]\mathrm{d}x}\left(I_T(0) + \int_0^t \frac{\sigma\mu\beta}{\Lambda} I(s)S(s)e^{-\int_0^s \left[\frac{\sigma\mu\beta\rho S(x)}{\Lambda}-\mu-\theta\right]\mathrm{d}x}\mathrm{d}s\right).$$

Integrating the third equation gives

$$\begin{aligned} I(t) = {} & e^{\int_0^t \left[\frac{(1-\sigma)\mu\beta S(x)}{\Lambda}-\mu-\gamma_I\right]\mathrm{d}x} \\ & \times\left(I(0) + \int_0^t \left[\frac{(1-\sigma)\mu\beta\rho}{\Lambda} I_T(s)S(s) + \epsilon\theta I_T(s)\right]e^{-\int_0^s \left[\frac{(1-\sigma)\mu\beta S(x)}{\Lambda}-\mu-\gamma_I\right]\mathrm{d}x}\mathrm{d}s\right). \end{aligned} \tag{3.1}$$

Since the initial conditions are non-negative, a sufficiently small constant $t_0 > 0$ exists such that $I_T(0) > 0$ and $I(0) > 0$ for all $t \in [0, t_0)$. Next, we need to prove that $I_T(t) > 0$ and $I(t) > 0$ for all $t \geq 0$. Otherwise, some $t_1 > 0$ exists such that $\min\{I_T(t_1), I(t_1)\} = 0$ and $\min\{I_T(t), I(t)\} > 0$ for all $t \in (0, t_1)$. Without loss of generality, we assume $I(t_1) = 0$. From the left-hand side of the equation (3.1), we have $I(t_1) = 0$, which contradicts $I(t_1) > 0$ obtained from the right-hand side of the equation. Therefore, $I(t) > 0$ for all $t \geq 0$. Similarly, we can easily show that $I_T(t) > 0$ for all $t \geq 0$.

We consider the combined form of the three equations to verify the boundedness of the system.

$$\frac{\mathrm{d}W}{\mathrm{d}t} = \Lambda - \mu S(t) - \mu I_T(t) - \frac{(1-\epsilon)\theta I_T(t)}{1+\delta I_T(t)} - (\mu+\gamma_I)I(t) \leq \Lambda - \mu W(t),$$

where $W(t) = S(t) + I_T(t) + I(t)$. By comparison with the differential inequality $\frac{\mathrm{d}W}{\mathrm{d}t} \leq \Lambda - \mu W(t)$, we conclude that $\limsup_{t\to\infty} W(t) \leq \Lambda/\mu$. Thus, the feasible region is given by

$$D = \{(S, I_T, I) \in \mathbb{R}^3_+ \mid S + I_T + I \leq \Lambda/\mu\},$$

which is positively invariant. This proof is complete.

□

3.2. Disease-free equilibrium and basic reproduction number

This subsection derives the DFE of Model (2.3), calculates R_0 using the NGM method, and analyzes the local and global stability conditions of the DFE.

Model (2.3) possesses a DFE, denoted $E_0 = (S_0, 0, 0)$, where $S_0 = \Lambda/\mu$. In Model (2.3), the infected compartments are I_T and I. According to the NGM method [39], the new infection terms $\mathcal{F}$ and the transition terms $\mathcal{V}$ for these compartments are defined as follows:

$$\begin{pmatrix} \frac{\mathrm{d}I_T}{\mathrm{d}t} \\ \frac{\mathrm{d}I}{\mathrm{d}t} \end{pmatrix} = \mathcal{F}(I_T, I) - \mathcal{V}(I_T, I) = \begin{pmatrix} \frac{\sigma\mu\beta(\rho I_T + I)S}{\Lambda} \\ \frac{(1-\sigma)\mu\beta(\rho I_T + I)S}{\Lambda} \end{pmatrix} - \begin{pmatrix} (\mu + \epsilon\theta)I_T + \frac{(1-\epsilon)\theta I_T}{1+\delta I_T} \\ (\mu + \gamma_I)I - \epsilon\theta I_T \end{pmatrix}.$$

Linearizing the system around $E_0 = (\Lambda/\mu, 0, 0)$, we obtain the Jacobian matrices of new infections F and transitions V as

$$F = D\mathcal{F}(I_T, I)\big|_{E_0} = \begin{pmatrix} \sigma\rho\beta & \sigma\beta \\ (1-\sigma)\rho\beta & (1-\sigma)\beta \end{pmatrix}, \quad V = D\mathcal{V}(I_T, I)\big|_{E_0} = \begin{pmatrix} \mu + \theta & 0 \\ -\epsilon\theta & \mu + \gamma_I \end{pmatrix}.$$

The NGM is given by $K = FV^{-1}$. We now compute V^{-1} and FV^{-1}

$$V^{-1} = \begin{pmatrix} \frac{1}{\mu+\theta} & 0 \\ \frac{\epsilon\theta}{(\mu+\theta)(\mu+\gamma_I)} & \frac{1}{\mu+\gamma_I} \end{pmatrix}, \quad FV^{-1} = \begin{pmatrix} Z & \frac{\sigma\beta}{\mu+\gamma_I} \\ Z_1 & \frac{(1-\sigma)\beta}{\mu+\gamma_I} \end{pmatrix}.$$

where

$$Z = \frac{\sigma\rho\beta}{\mu+\theta} + \frac{\epsilon\theta\sigma\beta}{(\mu+\theta)(\mu+\gamma_I)}, \text{ and } \quad Z_1 = \frac{(1-\sigma)\rho\beta}{\mu+\theta} + \frac{\epsilon\theta(1-\sigma)\beta}{(\mu+\theta)(\mu+\gamma_I)}.$$

The basic reproduction number R_0, defined as the spectral radius of the NGM $K = FV^{-1}$, is given by the dominant eigenvalue of K, obtained from solving its characteristic equation $\det(K - \lambda I) = 0$. By calculating the expression for R_0 as follows:

$$\mathcal{R}_0 = \frac{(1-\sigma)\beta}{\mu+\gamma_I} + \frac{\sigma\rho\beta}{\mu+\theta} + \frac{\epsilon\theta\sigma\beta}{(\mu+\theta)(\mu+\gamma_I)},$$

represents the average number of secondary infections generated by a single infectious case in a population of entirely susceptible individuals [40].

Theorem 3.2. *The DFE E_0 of Model (2.3) is locally asymptotically stable if $R_0 < 1$, and unstable if $R_0 > 1$.*

Proof. To analyze the local stability of E_0, we compute the Jacobian matrix of Model (2.3) evaluated at E_0. It is given by

$$J(E_0) = \begin{pmatrix} -\mu & -\beta\rho & -\beta \\ 0 & \sigma\beta\rho - \mu - \theta & \sigma\beta \\ 0 & \epsilon\theta - \beta\rho(\sigma - 1) & (1-\sigma)\beta - (\mu + \gamma_I) \end{pmatrix}.$$

By expanding the characteristic polynomial along the first column, it is straightforward to observe that $\lambda_1 = -\mu$ is an eigenvalue. The remaining two eigenvalues are the roots of the characteristic polynomial of the submatrix

$$J_1 = \begin{pmatrix} \sigma\beta\rho - \mu - \theta & \sigma\beta \\ \epsilon\theta - \beta\rho(\sigma - 1) & (1-\sigma)\beta - (\mu + \gamma_I) \end{pmatrix}.$$

The trace and determinant of J_1 are given by

$$\begin{aligned} \mathrm{Tr}(J_1) &= \sigma\beta\rho - \mu - \theta + (1-\sigma)\beta - \mu - \gamma_I, \\ \mathrm{Det}(J_1) &= (\mu+\theta)(\mu+\gamma_I) - \sigma\beta\rho(\mu+\gamma_I) - (1-\sigma)\beta(\mu+\theta) - \sigma\beta\epsilon\theta. \end{aligned}$$

From $\mathcal{R}_0 < 1$ and the non-negativity of all its components, we can draw two key conclusions. First, each individual term in the decomposition must be less than 1. We can obtain

$$(1-\sigma)\beta < \mu + \gamma_I, \quad \sigma\rho\beta < \mu + \theta.$$

Using these two inequalities, we can further deduce that $\mathrm{Tr}(J_1) < 0$. Second, multiplying both sides of $\mathcal{R}_0 < 1$ by $(\mu+\theta)(\mu+\gamma_I)$ (as epidemiological parameters are positive) gives

$$(\mu+\theta)(\mu+\gamma_I) > \sigma\beta\rho(\mu+\gamma_I) + (1-\sigma)\beta(\mu+\theta) + \sigma\beta\epsilon\theta.$$

From this, it follows that $\mathrm{Det}(J_1) > 0$.

The E_0 is locally asymptotically stable when $\mathrm{Tr}(J_1) < 0$ and $\mathrm{Det}(J_1) > 0$, which occurs precisely when $R_0 < 1$. Hence, the DFE is locally stable if and only if $R_0 < 1$. This proof is complete. □

Theorem 3.3. *The DFE E_0 of Model (2.3) is globally asymptotically stable if $R_0 < R^*$, where*

$$R^* = \frac{(1-\sigma)\beta(\mu+\theta) + (\mu+\epsilon\theta)[(\mu+\gamma_I) - (1-\sigma)\beta]}{(\mu+\theta)(\mu+\gamma_I)} < 1.$$

Proof. To prove the global asymptotic stability of E_0, we construct the following Lyapunov function $L = l_1 I_T + l_2 I$. To eliminate all coefficients of terms involving I in the inequality satisfied by $\frac{dL}{dt}$ (i.e., to make their sum zero), we set the coefficients of the Lyapunov function $L = l_1 I_T + l_2 I$ (where $l_1, l_2 > 0$ are undetermined coefficients) as follows: $l_1 = 1$, $l_2 = \frac{\sigma\beta}{(\mu+\gamma_I)-(1-\sigma)\beta}$.

Taking the derivative of L along the trajectories of system (2.3) gives

$$\begin{aligned} \frac{dL}{dt} &= l_1 \frac{dI_T}{dt} + l_2 \frac{dI}{dt} \\ &= \sigma\lambda S - (\mu+\epsilon\theta)I_T - \frac{(1-\epsilon)\theta I_T}{1+\delta I_T} + l_2[(1-\sigma)\lambda S + \epsilon\theta I_T - (\mu+\gamma_I)I] \\ &\le \sigma\lambda S_0 - (\mu+\epsilon\theta)I_T + l_2[(1-\sigma)\lambda S_0 + \epsilon\theta I_T - (\mu+\gamma_I)I] \\ &= \sigma\beta(\rho I_T + I) - (\mu+\epsilon\theta)I_T + \frac{\sigma\beta}{(\mu+\gamma_I)-(1-\sigma)\beta}[(1-\sigma)\beta(\rho I_T + I) + \epsilon\theta I_T - (\mu+\gamma_I)I] \\ &= \left[R_0 \cdot \frac{(\mu+\theta)(\mu+\gamma_I)}{(\mu+\gamma_I)-(1-\sigma)\beta}\right] I_T - \left[\frac{(1-\sigma)\beta(\mu+\theta) + (\mu+\epsilon\theta)[(\mu+\gamma_I)-(1-\sigma)\beta]}{(\mu+\gamma_I)-(1-\sigma)\beta}\right] I_T. \end{aligned}$$

Hence, $\frac{dL}{dt} \leq 0$ whenever

$$R_0 < \min\left(\frac{(1-\sigma)\beta(\mu+\theta)+(\mu+\epsilon\theta)[(\mu+\gamma_I)-(1-\sigma)\beta]}{(\mu+\theta)(\mu+\gamma_I)},\ 1\right).$$

To show that this upper bound is less than one, we compute

$$(1-\sigma)\beta(\mu+\theta)+(\mu+\epsilon\theta)[(\mu+\gamma_I)-(1-\sigma)\beta]-(\mu+\theta)(\mu+\gamma_I)=\theta(1-\epsilon)(\beta-\sigma\beta-\mu-\gamma_I).$$

Since $R_0 < 1$, we get $l_2 > 0$ and $\beta - \sigma\beta - \mu - \gamma_I > 0$; thus the expression above is negative, which implies that $R^* < 1$.

Furthermore, $\frac{dL}{dt} = 0$ if and only if (iff) $I_T = 0$ and $I = 0$. Therefore, the largest compact invariant set contained in $\{(I_T, I) : \frac{dL}{dt} = 0\}$ is the singleton E_0. By LaSalle's invariance principle [41], we conclude that the DFE is globally asymptotically stable whenever $R_0 < R^*$. This completes the proof. □

3.3. Existence of endemic equilibrium

In this subsection, we establish the existence of the endemic equilibrium for Model (2.3). Owing to the complexity of the expressions involved, we focus on proving the existence of the equilibrium rather than deriving its explicit form [42].

By defining $E^* = (S^*, I_T^*, I^*)$ as the endemic equilibrium and solving the steady-state equations of Model (2.3), we derive S^* and I^* in functions of I_T^*

$$S^* = \frac{\sigma\Lambda-(\mu+\epsilon\theta)\delta I_T^2+\sigma\Lambda\delta I_T-(\mu+\theta)I_T}{\sigma\mu(1+\delta I_T)}.$$

$$I^* = \frac{(\mu+\epsilon\theta)\delta\beta\rho I_T^3+(-\sigma\Lambda\delta\beta\rho+\mu\beta\rho+\mu\delta\Lambda+\epsilon\theta\Lambda\delta+\theta\beta\rho)I_T^2}{\Lambda\sigma\beta-(\mu+\epsilon\theta)\delta\beta I_T^2+\sigma\Lambda\beta\delta I_T-(\mu+\theta)\beta I_T}+\frac{(-\sigma\Lambda\beta\rho+\Lambda\mu+\Lambda\theta)I_T}{\Lambda\sigma\beta-(\mu+\epsilon\theta)\delta\beta I_T^2+\sigma\Lambda\beta\delta I_T-(\mu+\theta)\beta I_T}.$$

By summing the second and third equations of Model (2.3) and substituting the expressions above, we obtain a cubic equation in I_T^* of the form

$$f(I_T^*) = s(I_T^*)^3 + p(I_T^*)^2 + qI_T^* + r = 0,$$

where

$$\begin{aligned}
s &= (\mu+\epsilon\theta)[\sigma\delta^2\beta\mu-\delta^2\beta\mu-\delta^2\beta\epsilon\theta-\sigma\delta^2\beta\rho(\mu+\gamma_I)],\\
p &= (\mu+\epsilon\theta)[-2(\mu+\theta)\delta\beta+\Lambda\sigma\delta^2\beta+\sigma(\mu+\gamma_I)\delta\beta\rho]\\
&\quad+\sigma(\mu+\gamma_I)[-\Lambda\sigma\delta^2\beta\rho+\mu\beta\rho\delta+\Lambda\mu\delta^2+\epsilon\theta\Lambda\delta^2+\theta\beta\rho\delta],\\
q &= \Lambda\sigma\delta\beta\theta(1-\epsilon)+2\Lambda\sigma\delta\beta(\mu+\epsilon\theta)-\mu\delta\\
&\quad-(\mu+\theta)^2\beta+\sigma(\mu+\gamma_I)(-2\Lambda\sigma\delta\beta\rho+\mu\beta\rho+2\mu\delta\Lambda+\epsilon\theta\delta\Lambda+\theta\beta\rho+\theta\Lambda\delta),\\
r &= \Lambda\sigma\beta(\mu+\theta)+\sigma(\mu+\gamma_I)(-\Lambda\sigma\beta\rho+\mu\Lambda+\theta\Lambda)-\mu-(1-\epsilon)\theta.
\end{aligned}$$

Clearly, the leading coefficient s is always negative. We observe that the sign of the constant term r corresponds to the sign of $R_0 - 1$: when $R_0 < 1$, $r > 0$; and when $R_0 > 1$, $r < 0$. According to Descartes' rule [43], the number of positive real roots equals the number of sign changes in the coefficients or is less than that given by an even number. Hence, the number of endemic equilibria depends on the values of the system's parameters and R_0, as shown in Table 2.

Table 2. Existence of the endemic equilibrium of Model (2.3).

Case	s	p	q	r	R_0	Number of changes in sign	Number of positive roots
1	-	+	+	+	$R_0 > 1$	1	1
2	-	+	+	-	$R_0 < 1$	2	0, 2
3	-	+	-	+	$R_0 > 1$	3	1, 3
4	-	+	-	-	$R_0 < 1$	2	0, 2
5	-	-	+	+	$R_0 > 1$	1	1
6	-	-	+	-	$R_0 < 1$	2	0, 2
7	-	-	-	+	$R_0 > 1$	1	1
8	-	-	-	-	$R_0 < 1$	0	0

3.4. Existence of backward bifurcation

As shown in Table 2, Model (2.3) undergoes a backward bifurcation. In this subsection, we provide a formal proof of the existence of this backward bifurcation.

Theorem 3.4. *Two positive equilibria occur in Model (2.3) when $R_0 < 1$; at $R_0(\beta) = 1$, a backward bifurcation occurs.*

Proof. We will now apply the center manifold theorem, as described by Castillo-Chavez and Song [44], to demonstrate the existence of a backward bifurcation. First, we set $x_1 = S$, $x_2 = I_T$, and $x_3 = I$. The system of equations corresponding to Model (2.3) is given by

$$\begin{aligned}
\frac{\mathrm{d}x_1}{\mathrm{d}t} &= \Lambda - \lambda(t)x_1 - \mu x_1,\\
\frac{\mathrm{d}x_2}{\mathrm{d}t} &= \sigma\lambda(t)x_1 - \mu x_2 - \epsilon\theta x_2 - \frac{(1-\epsilon)\theta x_2}{1+\delta x_2},\\
\frac{\mathrm{d}x_3}{\mathrm{d}t} &= (1-\sigma)\lambda(t)x_1 + \epsilon\theta x_2 - (\mu+\gamma_I)x_3,
\end{aligned} \tag{3.2}$$

where $\lambda(t) = \mu\beta(\rho x_2(t) + x_3(t))/\Lambda$.

We choose β as a bifurcation parameter. The critical value β^*, satisfying $R_0(\beta^*) = 1$, is

$$\beta^* = \frac{(\mu+\theta)(\mu+\gamma_I)}{\sigma\rho(\mu+\gamma_I) + \epsilon\theta\sigma + (1-\sigma)(\mu+\theta)}.$$

The DFE is given by $E_0^* = \left(x_1^*, 0, 0\right)$, where $x_1^* = \Lambda/\mu$. The linearization at the DFE for $\beta = \beta^*$ is given by (see (3.2))

$$J_{(\beta^*)} = \begin{pmatrix} -\mu & -\beta^*\rho & -\beta^* \\ 0 & \sigma\beta^*\rho - \mu - \theta & \beta^*\sigma \\ 0 & \epsilon\theta - \beta^*\rho(\sigma-1) & (1-\sigma)\beta^* - (\mu+\gamma_I) \end{pmatrix}.$$

The eigenvalues of the Jacobian matrix at the DFE are found by solving the characteristic equation $\left|J_{(\beta^*)} - \lambda I_{3\times 3}\right| = 0$. The eigenvalues are given by $\lambda_1 = -\mu, \lambda_2 = 0$, and $\lambda_3 = \sigma\beta^*\rho + (1-\sigma)\beta^* - (\mu +$

$\theta)-(\mu+\gamma_I)$. Hence, 0 is a simple eigenvalue. To compute the right eigenvector $\vec{\omega}$, we solve $J_{(\beta^*)}\vec{\omega}=0$, assuming $\vec{\omega}=(x,y,z)$. Similarly, the left eigenvector $\vec{v}$ is computed by solving $\vec{v}J_{(\beta^*)}=0$. We set $\vec{v}=(v_1,v_2,v_3)$. By calculation, we obtain the following expression:

$$\vec{\omega}=\left(\frac{(\mu+\theta)\beta^*}{\mu},-\beta^*\sigma,\beta^*\sigma\rho-(\mu+\theta)\right),$$

$$\vec{v}=\left(0,\beta^*\rho(\sigma-1)-\epsilon\theta,\beta^*\sigma\rho-(\mu+\theta)\right).$$

Using the algebraic operations for a and b as described in Castillo-Chavez and Song [44], we compute

$$a=\sum_{k,i,j=1}^{3}v_k w_i w_j\frac{\partial^2 f_k}{\partial x_i\partial x_j}(E_0),\quad b=\sum_{k,i=1}^{3}v_k w_i\frac{\partial^2 f_k}{\partial x_i\partial\beta^*}(E_0).$$

By calculation, we obtain the following expression:

$$a=[\beta^*\rho(\sigma-1)-\epsilon\theta]\cdot\left[2\frac{(\mu+\theta)\beta^*}{\mu}(-\beta^*\sigma)\frac{\beta^*\sigma\rho\mu}{\Lambda}+2\frac{(\mu+\theta)\beta^*}{\mu}(\beta^*\sigma\rho-\mu-\theta)\frac{\beta^*\sigma\mu}{\Lambda}+\beta^{*2}\sigma^2(-2\delta\theta(1-\epsilon))\right],$$

$$b=[\beta^*\rho(\sigma-1)-\epsilon\theta]\cdot\left[-\beta^*\sigma^2\rho+(\beta^*\sigma\rho-\mu-\theta)\sigma\right]+(\beta^*\sigma\rho-\mu-\theta)\cdot\left[-\beta^*\sigma\rho(1-\sigma)+(\beta^*\sigma\rho-\mu-\theta)(1-\sigma)\right].$$

Substituting β^* into the expressions for a and b, we find that $a>0$ and $b>0$. According to the Castillo-Chavez and Song bifurcation theorem [44], this implies the existence of backward bifurcation at $R_0(\beta)=1$. This completes the proof. □

Remark 3.5. *The occurrence of a backward bifurcation indicates that achieving $R_0=1$ may not guarantee elimination of the disease. Numerical simulations in Section 4 further demonstrate the occurrence of this phenomenon.*

3.5. Uniform persistence of the disease

Systemic persistence indicates the disease cannot be eradicated and will remain endemic above a certain threshold, complementing the scenario of a stable DFE and providing a theoretical basis for classifying the long-term dynamics in numerical simulations. In this subsection, we aim to prove the consistent persistence of Model (2.3) conditional on $R_0>1$, i.e., when $R_0>1$, disease persists in the population [45].

Theorem 3.6. *If $R_0>1$, the disease in Model (2.3) is uniformly persistent. That is, a positive constant $\epsilon_0>0$ exists such that, for all initial values $(S(0),I_T(0),I(0))\in\mathbb{R}^3_+$, the solutions of Model (2.3) satisfy*

$$\liminf_{t\to\infty}S(t)\geq\epsilon_0,\quad\liminf_{t\to\infty}I_T(t)\geq\epsilon_0,\quad\liminf_{t\to\infty}I(t)\geq\epsilon_0,$$
$$\limsup_{t\to\infty}S(t)\leq\frac{\Lambda}{\mu},\quad\limsup_{t\to\infty}I_T(t)\leq\frac{\Lambda}{\mu},\quad\limsup_{t\to\infty}I(t)\leq\frac{\Lambda}{\mu}.$$

Proof. Define

$$X=\{(S,I_T,I)\mid S\geq 0,\ I_T\geq 0,\ I\geq 0\},$$

$$X_0 = \{(S, I_T, I) \mid S \geq 0,\ I_T \geq 0,\ I > 0\},$$
$$\partial X_0 = X \setminus X_0.$$

To prove uniform persistence of the system (2.3) with respect to $(X_0, \partial X_0)$, we first note that both X and X_0 are positively invariant due to the structure of the model. Additionally, ∂X_0 is relatively closed in X, and the system is point-dissipative. Set

$$M_\partial = \{(S(0), I_T(0), I(0)) :\ (S(t), I_T(t), I(t)) \in \partial X_0,\ \forall t \geq 0\}.$$

We show that $M_\partial = \{(S, 0, 0) \mid S \geq 0\}$. Assume that $(S(0), I_T(0), I(0)) \in M_\partial$. It is sufficient to demonstrate that $I_T(t) = 0$ and $I(t) = 0$ for all $t \geq 0$. Otherwise, $t_0 \geq 0$ exists such that either $I_T(t_0) > 0,\ I(t_0) = 0$ or $I_T(t_0) = 0$, or $I(t_0) > 0$. For the case $I_T(t_0) > 0$ and $I(t_0) = 0$, we get

$$\frac{dI}{dt}(t_0) = (1-\sigma)\frac{\mu\beta}{\Lambda}\rho I_T(t_0)S(t_0) + \epsilon\theta I_T(t_0) > 0.$$

Therefore, a positive constant $\epsilon_0 > 0$ exists such that $I_T(t) > 0$ for $t_0 < t < t_0 + \epsilon_0$. This proves that $(S(t), I_T(t), I(t)) \notin \partial X_0$ for $t_0 < t < t_0 + \epsilon_0$, which contradicts the assumption that $(S(0), I_T(0), I(0)) \in M_\partial$. Similar contradictions arise in the remaining cases, leading to the conclusion that $M_\partial = \{(S, 0, 0) \mid S \geq 0\}$.

It is worth noting that E_0 is globally asymptotically stable in Int M_∂ and forms an isolated invariant set in X. Therefore, $W_s(E_0) \cap X_0 = \emptyset$. Every orbit in M_∂ converges to E_0, and E_0 is acyclic in M_∂. We claim that $W_s(E_0) \cap X_0 = \emptyset$ for $R_0 > 1$. Assuming the contrary, we get $W_s(E_0) \cap X_0 \neq \emptyset$, which leads to the existence of a positive solution for the system $(S(t), I_T(t), I(t))$, where $(S(0), I_T(0), I(0)) \in X_0$. Then $(S(t), I_T(t), I(t)) \to E_0$ as $t \to \infty$ for $R_0 > 1$.

For $R_0 > 1$, we can choose an $\eta > 0$ small enough such that $R_0(1-\eta) > 1$. When t is sufficiently large, we then have $m - \eta m \leq S(t) \leq m + \eta m$. Therefore, we can deduce that the following inequality is valid:

$$\frac{dI_T}{dt}(t) \geq \sigma\lambda(m - \eta m) - (\mu + \epsilon\theta)I_T - (1-\epsilon)\theta I_T,$$
$$\frac{dI}{dt}(t) \geq (1-\sigma)\lambda(m - \eta m) + \epsilon\theta I_T - (\mu + \gamma_I)I.$$

Thus, we get a comparison system for the original system, and when the initial values are the same, the eigenroot of the comparison system is smaller than the eigenroot of the original system. Therefore, the stability of the comparison system can be judged.

$$\frac{d\hat{I}_T}{dt}(t) = \sigma\lambda(m - \eta m) - (\mu + \epsilon\theta)I_T - (1-\epsilon)\theta I_T,$$
$$\frac{d\hat{I}}{dt}(t) = (1-\sigma)\lambda(m - \eta m) + \epsilon\theta I_T - (\mu + \gamma_I)I.$$

Define

$$M = \begin{pmatrix} \sigma m(1-\eta)\frac{\mu\beta\rho}{\Lambda} - \mu - \theta - \lambda & \sigma(m - \eta m)\frac{\mu\beta}{\Lambda} \\ (1-\sigma)m(1-\eta)\frac{\mu\beta\rho}{\Lambda} + \epsilon\theta & (1-\sigma)(m - \eta m)\frac{\mu\beta}{\Lambda} - (\mu + \gamma_I) - \lambda \end{pmatrix}.$$

Recall that the stability modulus of an $n \times n$ matrix M, denoted $s(M)$, is defined as $s(M) = \max\{\text{Re}\,\lambda : \lambda \text{ is an eigenvalue of } M\}$, and the characteristic polynomial is $|M - \lambda E| = \lambda^2 + a_1\lambda + a_2$, where

$$a_1 = -\Big[\sigma m(1-\eta)\frac{\mu\beta\rho}{\Lambda} - \mu - \theta + (1-\sigma)(m-\eta m)\frac{\mu\beta}{\Lambda} - (\mu+\gamma_I)\Big],$$
$$a_2 = (\mu+\theta)(\mu+\gamma_I)(1-R_0(1-\eta)).$$

When $R_0(1-\eta) > 1$, $a_2 < 0$, meaning that $s(M)$ is a simple positive eigenvalue of M, corresponding to a (componentwise) positive eigenvector. This contradicts the assumption that $(S(t), I_T(t), I(t)) \to E_0$ as $t \to \infty$. Thus $W_s(E_0) \cap X_0 = \emptyset$ for $R_0 > 1$, proving that Model (2.3) is uniformly persistent. The proof of the theorem is now complete. □

Figure 2 presents a bifurcation diagram summarizing the global dynamics of Model (2.3) in relation to R_0. Specifically, when $0 < R_0 < R^*$, as described in Theorem 3.3, the DFE is globally asymptotically stable, indicating that the disease will eventually die out. For $R^* < R_0 < R_C$, the system's qualitative behavior remains unclear and requires further investigation. When $R_C < R_0 < 1$, as described in Theorem 3.4, Model (2.3) may admit two positive equilibria, suggesting the occurrence of backward bifurcation. In this case, the long-term outcome (whether the disease persists or vanishes) depending on the initial conditions. Finally, for $R_0 > 1$, as established in Theorem 3.6, the system exhibits uniform persistence, implying that the disease will persist over time.

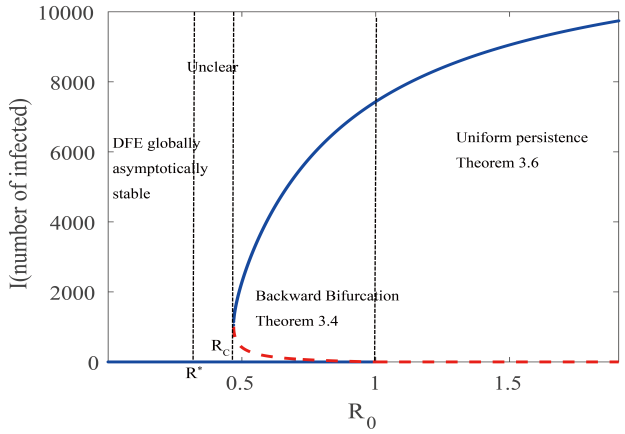

Figure 2. The global dynamics of Model (2.3) associated with R_0. Specifically, Theorem 3.3 establishes the extinction of the disease when $0 < R_0 < R^*$, Theorem 3.4 addresses the bistability and backward bifurcation phenomena in the interval $R_C < R_0 < 1$, and Theorem 3.6 proves the uniform persistence of the disease when $R_0 > 1$.

4. Numerical experimentations

To validate and further substantiate the theoretical findings, numerical simulations were performed using MATLAB R2020b to systematically investigate the combined effects of isolation resource availability and compliance on the dynamics of an epidemic's transmission. The parameter δ, representing the level of isolation resources, is based on COVID-19 outbreak data published by the

Hubei Provincial Health Commission, ranging from 0.0001 to 0.01, where $1/\delta$ denotes the maximum isolation capacity [46]. For instance, a value of $\delta = 0.0001$ corresponds to a maximum isolation capacity of 10,000 beds. Following the data provided by Gao et al., the isolation compliance parameter ϵ is chosen as 0.1, 0.3, and 0.5 [26].

We first analyze the influence of varying isolation resource levels on infection dynamics under fixed compliance scenarios. The simulation results indicate that, for a given compliance rate, increasing the availability of isolation resources significantly reduces the infection burden, highlighting the positive role of resource input in epidemic control. We then examine the effects of varying compliance levels under different resource conditions, which reveal a synergistic interaction between isolation compliance and resource availability in modulating transmission dynamics. Notably, the simulations suggest that under conditions of resource scarcity, higher compliance may paradoxically lead to an elevated infection risk, reflecting atypical transmission behavior. Finally, we analyze the impact of isolation time delays on the spread of the disease. The results underscore the critical importance of timely implementation of isolation measures for effective epidemic mitigation.

4.1. Impact of isolation capacity

To better understand how limited isolation resources affect the epidemic's spread and control strategies, we perform numerical simulations to investigate the system's dynamics with respect to the resource-related parameter δ. Specifically, on the basis of the biologically meaningful parameter combinations provided in Table 1, we fix the isolation compliance parameter at $\epsilon = 0.3$ and conduct simulations for various values of δ, where $1/\delta$ denotes the maximum available isolation capacity. We use the transmission probability β as the bifurcation parameter to investigate changes in the system's dynamic response and propagation behavior under varying levels of isolation resources.

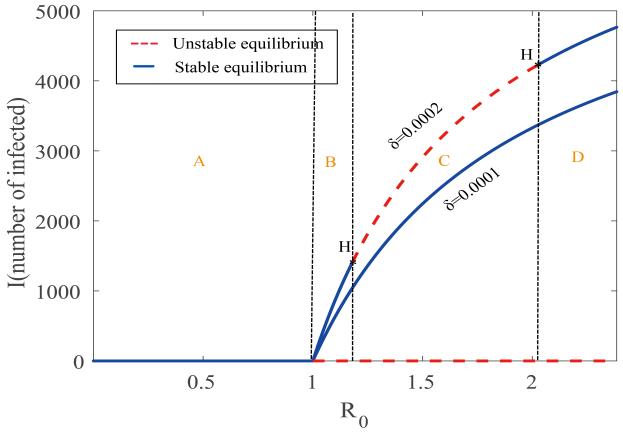

Figure 3. Bifurcation diagram of (R_0, I) for different values of the isolation capacity parameter δ ($\delta = 0.0001$ and $\delta = 0.0002$), where blue solid lines represent stable equilibria, red dashed lines represent unstable equilibria, and black dots labeled with "H" indicate that the system undergoes Hopf bifurcation. According to the different phenomena occurring in the system, R_0 is divided into four regions (A, B, C, D).

We first fix the isolation resource parameter at $\delta = 0.0001$ and $\delta = 0.0002$, and allow β to vary continuously within the interval [0.0001, 0.5]. The resulting bifurcation diagram, as shown in Figure 3,

illustrates the equilibrium transitions of the system under different transmission intensities.

When the isolation resource parameter $\delta = 0.0001$, the system exhibits typical forward bifurcation behavior. As shown in Figure 3, for Model (2.3), when R_0 increases from below 1 to above 1, a stable positive equilibrium emerges, while the DFE becomes unstable. Specifically, when $R_0 < 1$, the number of infected individuals gradually decreases to zero over time, leading to disease extinction. When $R_0 > 1$, the number of infected individuals increases as R_0 rises, and the epidemic evolves into a sustained endemic state. When $R_0 < 1$, the DFE is the only stable equilibrium, indicating that effective control is achievable if the R_0 remains below the threshold through appropriate interventions.

In Figure 3, for $\delta = 0.0002$, the system exhibits a stable DFE when $R_0 < 1$ (Region A), causing the disease to eventually disappear as the infected individuals tend to zero. This indicates that stable epidemic control can be achieved by maintaining $R_0 < 1$ (Figure 4(a, b)). When $1 < R_0 < 1.18274$ (Region B), the system exhibits a stable EE, while the DFE becomes unstable, and the outbreak evolves into an endemic state (Figure 4(c, d)). For $1.18274 < R_0 < 2.01545$ (Region C), the system no longer tends to a stable equilibrium but instead exhibits an unstable DFE along with an unstable EE. At this stage, the system experiences a Hopf bifurcation, leading to a limit cycle with persistent oscillations in the infected population. This behavior indicates that the system is sensitive to the initial conditions, with the epidemic exhibiting periodic fluctuations. In practical scenarios, disease transmission is subject to the influence of multiple factors. Under resource constraints, recurrent outbreaks occur frequently, and the scales of infection are characterized by multiple peaks (Figure 4(e, f)). Finally, when $R_0 > 2.01545$ (Region D), the system stabilizes at a stable endemic equilibrium, despite the instability of the DFE, leading to a convergence to a stable epidemiological state with no cyclic fluctuations, although outbreaks persist (Figure 4(g, h)).

These results indicate that while maintaining $R_0 < 1$ is crucial for controlling outbreaks effectively, the system may still exhibit unstable dynamics and cyclic outbreaks when $R_0 > 1$, particularly near the Hopf bifurcation threshold. Therefore, public health interventions must not only aim to reduce R_0 below the epidemic threshold but also consider the potential dynamic uncertainties within the critical interval. Recognizing this is vital to preventing recurrent or fluctuating outbreaks driven by the system's intrinsic instability.

We set the isolation resource parameter to $\delta = 8 \times 10^{-4}$ and allow β to vary continuously within the interval [0.0001, 0.4]. The corresponding bifurcation diagram, shown in Figure 5, illustrates the changes in the system's equilibrium states under varying transmission intensities.

Unlike Figure 3, Figure 5 illustrates backward bifurcation, where solutions originating from any positive equilibrium (EE) with $R_0 < 1$ converge to DFE. Specifically, when $R_0 < 0.8822$ (Region A), the system converges to the DFE, leading to disease extinction. For $0.8822 < R_0 < 1$ (Region B), the system exhibits two unstable EEs. For instance, when $\beta = 0.2$ ($R_0 = 0.9538$), the unstable EEs are $E_1^* = (154752.6633, 302.4789, 353.0193)$ and $E_2^* = (97901.5292, 3543.3520, 3528.3008)$ (Figure 6(a, d)). An EE emerges when $R_0 > 1$. Specifically, when $1 < R_0 < 1.1441$ (Region C), the EE is unstable, and the system experiences a Hopf bifurcation, leading to a limit cycle (Figure 6(b, e)). This suggests that the number of infections will oscillate over time due to the initial conditions, potentially leading to repeated outbreaks. Consequently, public health strategies must consider long-term prevention, cyclical resource allocation, and not solely one-time emergency interventions. When $R_0 > 1.1388$ (Region D), the EE becomes stable (Figure 6(c, f)), indicating that the disease will persist within the population.

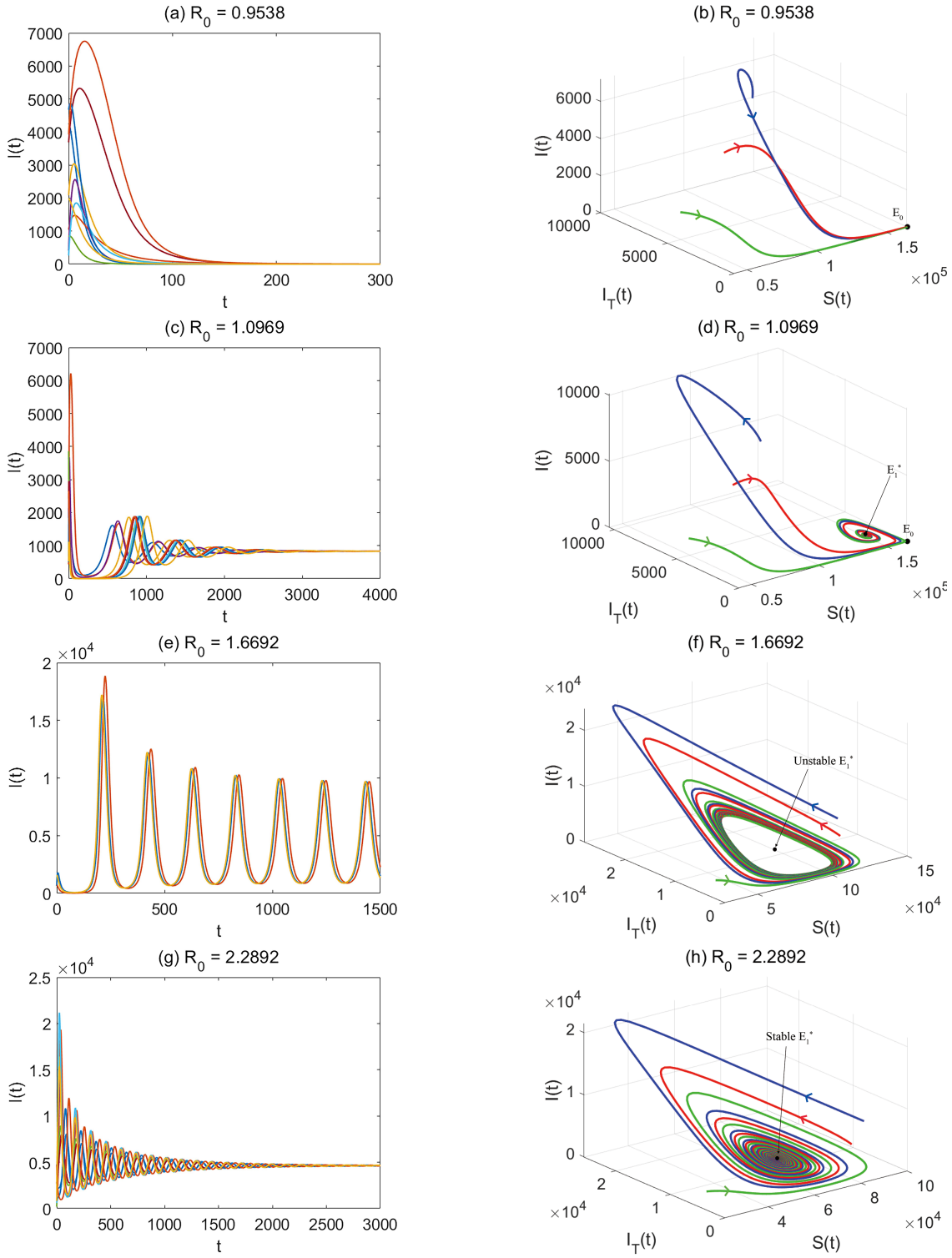

Figure 4. The plots of each region (A, B, C, D) divided at $\delta = 0.0002$ for Figure 3: The left panel of each set is a timing plot and the right panel is a phase plot. Each set of plots has the same R_0.

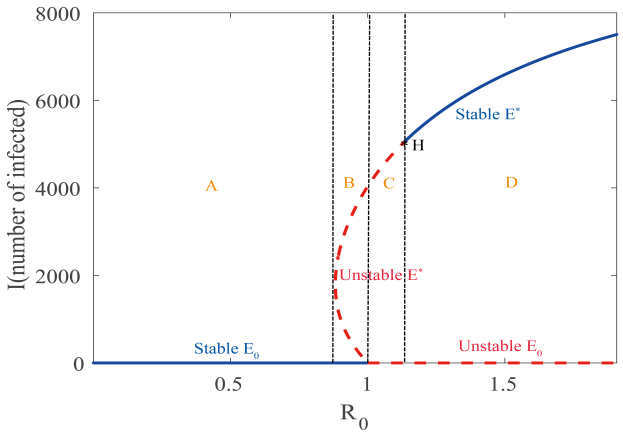

Figure 5. Bifurcation diagram of (R_0, I) for different values of the isolation capacity parameter δ ($\delta = 0.0008$), where blue solid lines represent stable equilibria, red dashed lines represent unstable equilibria, and black dots labeled with "H" indicate that the system undergoes Hopf bifurcation. According to the different phenomena occurring in the system, R_0 is divided into four regions (A, B, C, D).

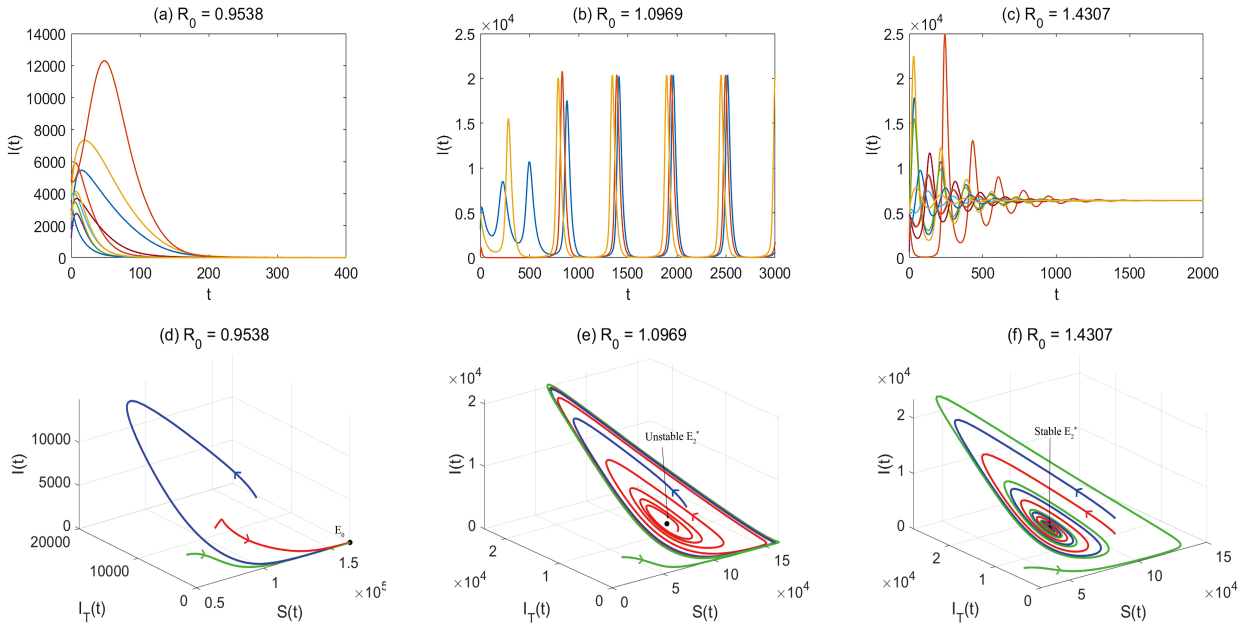

Figure 6. The plots of each region (B, C, D) divided at $\delta = 0.0008$ for Figure 5: The first row shows the time series diagrams, while the second row displays the phase diagrams. The upper and lower diagrams share the same basic reproduction number (R_0).

We set the isolation resource parameter as $\delta = 0.0015$ and allow β to vary continuously from 0.0001 to 0.4. The bifurcation diagram corresponding to these parameter values is shown in Figure 7, illustrating the changes in the system's equilibrium states under varying transmission intensities.

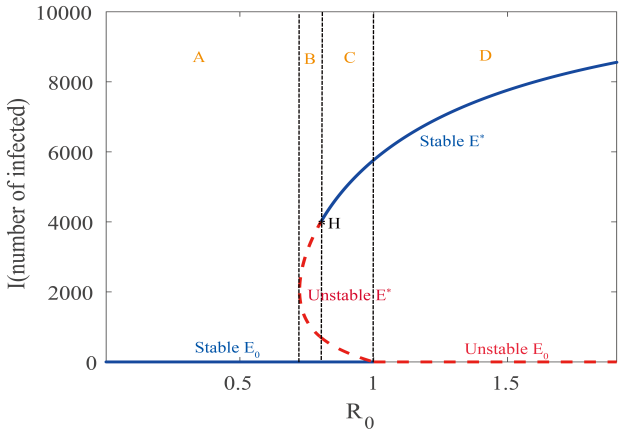

Figure 7. Bifurcation diagram of (R_0, I) for different values of the isolation capacity parameter δ ($\delta = 0.0015$), where blue solid lines represent stable equilibria, red dashed lines represent unstable equilibria, and black dots labeled with "H" indicate that the system undergoes Hopf bifurcation. According to the different phenomena occurring in the system, R_0 is divided into four regions (A, B, C, D).

The bifurcation diagram is shown in Figure 7. When $R_0 < 0.7229$ (Region A), for any positive initial condition, the system converges to the DFE, leading to the disease's extinction. In the range $0.7229 < R_0 < 0.8026$ (Region B), the system has two unstable EEs, yet the solution still converges to the DFE, indicating that the disease remains controllable within this interval (Figure 8(a, d)). When $0.8026 < R_0 < 1$ (Region C), both a stable E_2^* and an unstable E_1^* emerge, forming a bistable structure (Figure 8(b, e)). Specifically, the stable EE, E_2^*, coexists with the stable DFE, E_0. For instance, when $\beta = 0.2$ and $R_0 = 0.9538$, the system has two EEs: $E_1^* = (161412.8194, 5761.1777, 5451.9172)$ and $E_2^* = (161412.8194, 94.1738, 112.0152)$, with E_2^* being the stable EE. This behavior suggests that the final state of the system depends on the initial conditions, where the extinction or persistence of the disease is closely tied to the early infection dynamics. When $R_0 > 1$ (Region D), the system has a single stable EE, and the disease continues to spread (Figure 8(c, f)).

We set the isolation resource parameter to $\delta = 0.015$ and allow β to vary continuously from 0.0001 to 0.4. The resulting backward bifurcation diagram, shown in Figure 9, is a typical backward bifurcation diagram.

Upon examining Figure 9, when $R_0 < 0.5150$ (Region A), the system only has a stable DFE, and solutions starting from any positive equilibrium converge to the DFE (Figure 10(a, d)). In the range $0.4688 < R_0 < 1$ (Region B), the system possesses two positive equilibria. The stable DFE coexists with the stable E_2^*, resulting in a bistable state (Figure 10(b, e)). The ultimate trajectory of the epidemic depends on the initial conditions. For instance, when $\beta = 0.14$ ($R_0 = 0.6677$), Model (2.3) exhibits two positive equilibria: $E_1^* = (162444.3073, 99.2235, 103.2082)$ and $E_2^* = (97042.6144, 5422.6596, 4975.2892)$, where E_1^* is unstable and E_2^* is stable. This suggests that the stable E_2^* coexists with the stable DFE E_0. When $R_0 > 1$ (Region C), the EE becomes stable

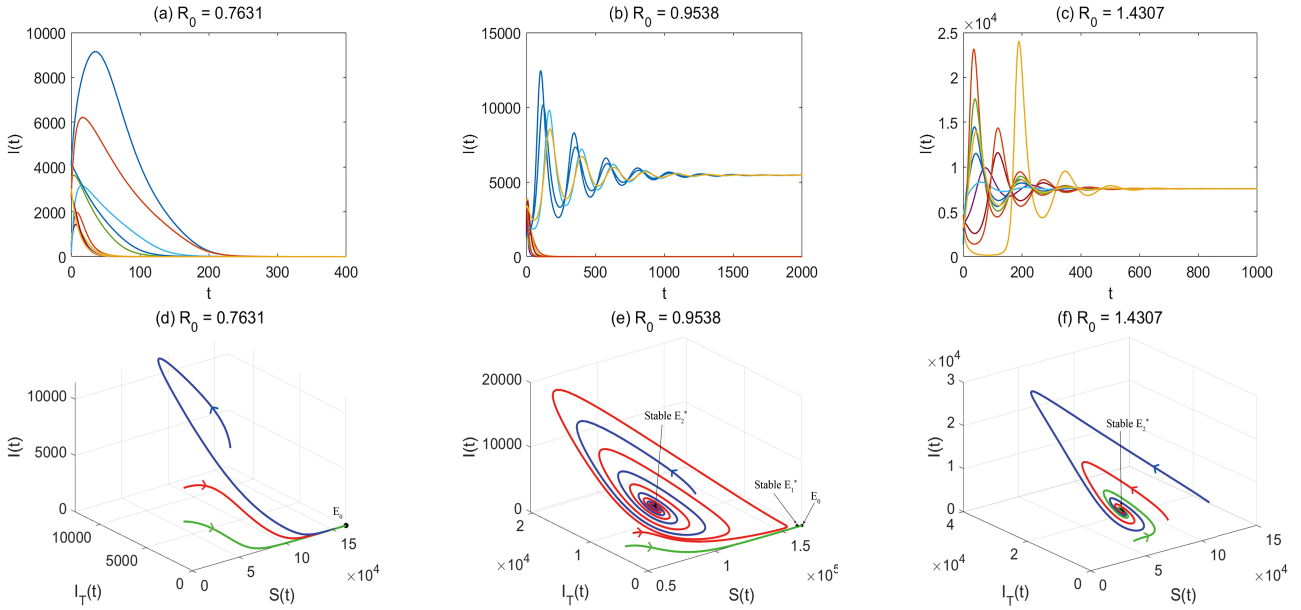

Figure 8. The plots of each region (B, C, D) divided at $\delta = 0.0015$ for Figure 7: The first row shows the time series diagrams, while the second row displays the phase diagrams. The upper and lower diagrams share the same basic reproduction number (R_0).

(Figure 10(c, f)), indicating that the disease will persist in the population over time. The existence of a backward bifurcation highlights that simply reducing R_0 below 1 is insufficient for eradication of the disease; more stringent control measures are required for disease extinction.

4.2. Comprehensive effects of isolation capacity and compliance

This section further investigates the influence of variations in isolation resources on the system's bifurcation structure and the infection level. Figure 11(a) illustrates the changes in the bifurcation diagram under different isolation capacities (characterized by δ), while Figure 11(b) illustrates that changes in isolation resources significantly affect the total number of infected cases $I + I_T$.

As shown in Figure 11(a), for a fixed isolation compliance rate ($\varepsilon = 0.3$), increasing the maximum available isolation resources (i.e., decreasing δ) causes the turning point to approach 1. This shift suggests that the disease becomes more controllable. Additionally, the domain of attraction of the DFE expands, which is evident from the fact that Point c lies above Point b, which, in turn, lies above the reference point in Figure 11(a), and the overall infection level decreases. These results indicate that enhancing the isolation capacity reduces the prevalence of the infection and improves the effectiveness of epidemic control.

Figure 11(b) further demonstrates that although δ does not influence R_0 ($R_0 = 1.9076 > 1$), it significantly impacts the total number of $I + I_T$, when all other parameters are held constant. Specifically, an increase in δ (corresponding to a reduction in isolation resources) leads to a marked rise in the infection burden, as indicated by the ordering $a > b > c > d$ in Figure 11(b). Conversely, decreasing δ (i.e., enhancing the isolation capacity) substantially lowers the number of infections and alleviates pressure on both social and healthcare systems.

To systematically evaluate the combined effects of isolation compliance and isolation resource

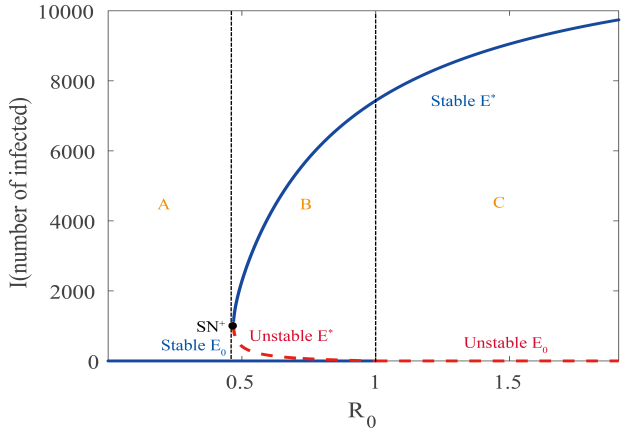

Figure 9. Bifurcation diagram of (R_0, I) for different values of the isolation capacity parameter δ ($\delta = 0.015$), where blue solid lines represent stable equilibria, red dashed lines represent unstable equilibria, and black dots labeled with "SN^+" represent a saddle-node bifurcation. According to the different phenomena occurring in the system, R_0 is divided into four regions (A, B, C).

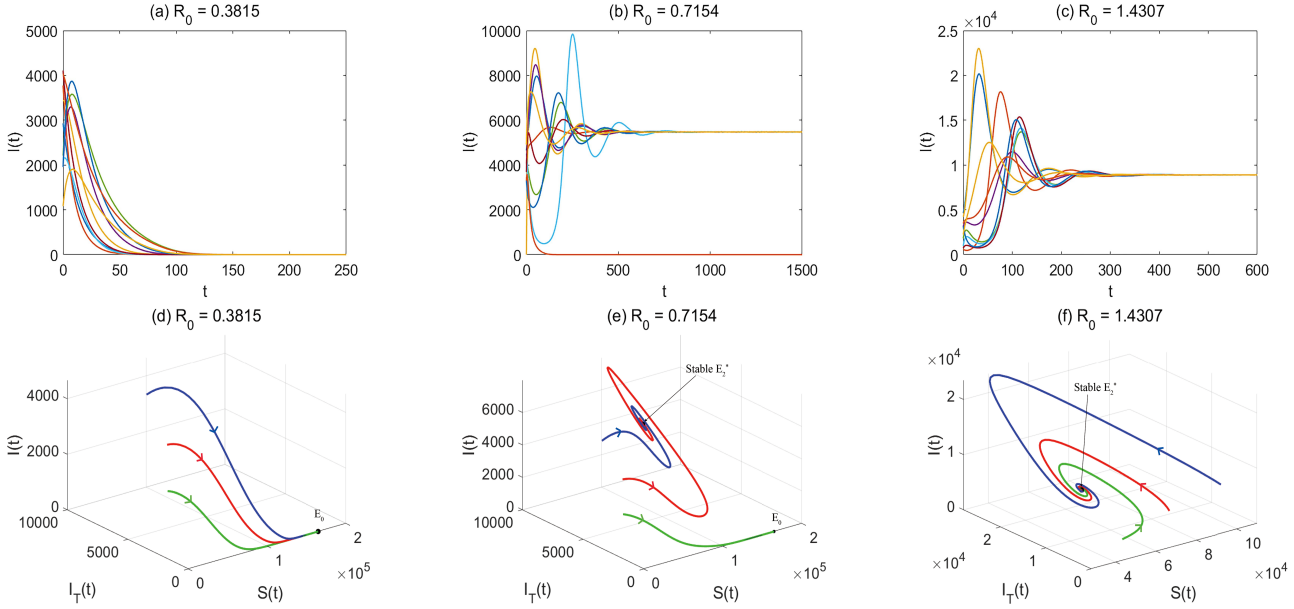

Figure 10. Analytical plot of regions (A, B, C), divided by $\delta = 0.015$, corresponding to Figure 9: The first row shows the time series diagrams, while the second row displays the phase diagrams. The upper and lower diagrams share the same basic reproduction number (R_0).

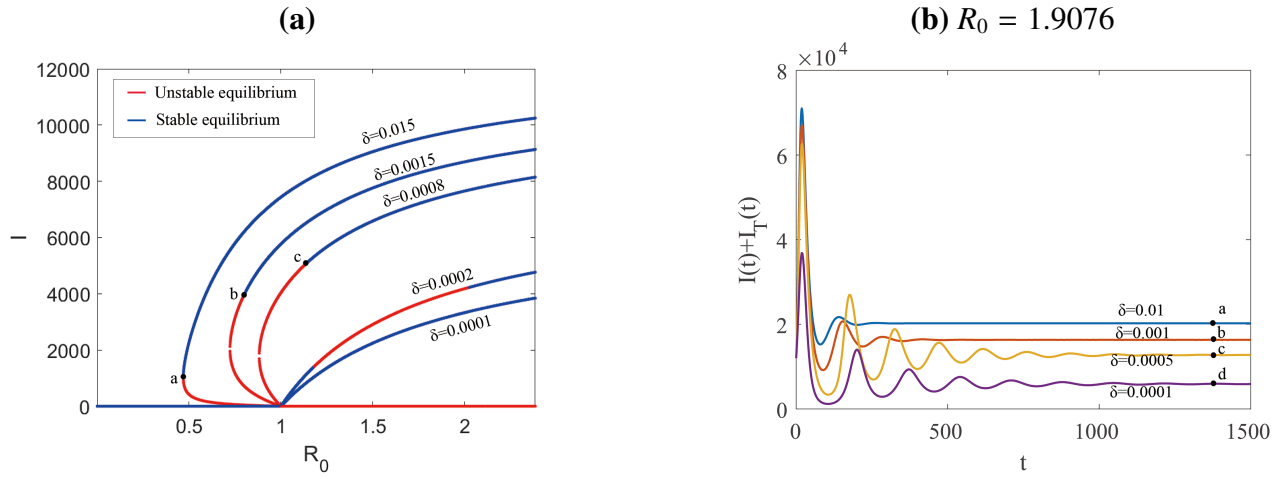

Figure 11. (a) Bifurcation diagram of the effect of different parameters δ ($1/\delta$ denotes the maximum isolation capacity) in the (R_0, I) plane. This demonstrates the fundamental difference in bifurcation behavior between scenarios of abundant and scarce isolation resources, revealing the critical role of resource thresholds in disease control. (b) Results for $R_0 = 1.9076$, varying isolation resources ($\delta = 0.01, 0.001, 0.0005, 0.0001$), and observing the timing diagram of $I + I_T$ over time.

availability on the dynamics and control of infectious diseases, we conducted simulations to analyze how changes in compliance influence the disease's dynamics under varying levels of isolation capacity ($\delta = 0.01$, 0.001, and 0.0001). This was achieved by jointly adjusting the isolation resource parameter δ and the isolation compliance parameter, where $(1 - \varepsilon)$ denotes the compliance rate to isolation measures.

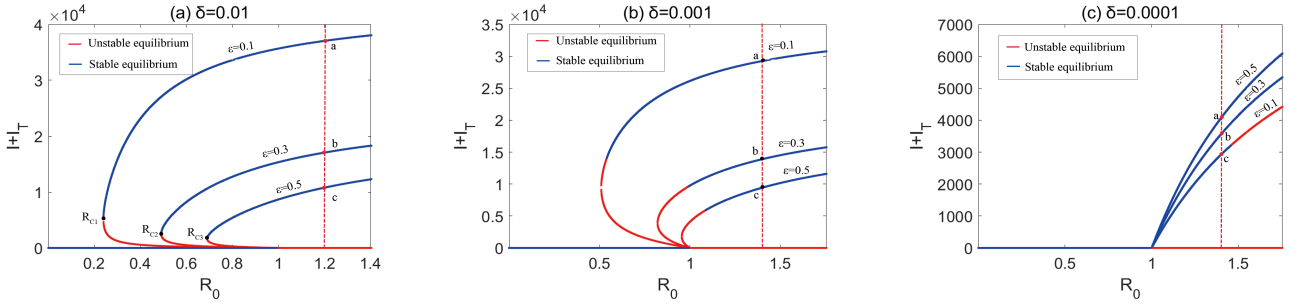

Figure 12. The effect of different isolation compliance ($\epsilon = 0.1$, $\epsilon = 0.3$, $\epsilon = 0.5$) on the total number of infections($I + I_T$) at different isolation capacities ($\delta = 0.01$ corresponds to 100 beds, $\delta = 0.001$ corresponds to 1000 beds, and $\delta = 0.0001$ corresponds to 10,000 beds) in the $(R_0, I + I_T)$ plane. This reveals the paradoxical phenomenon of high compliance actually accelerating transmission during resource scarcity, underscoring the necessity for coordinated interventions targeting both resources and behavior.

The subplots (a), (b), and (c) in Figure 12 correspond to $\delta = 0.01$, $\delta = 0.001$, and $\delta = 0.0001$, representing low, moderate, and high levels of isolation resources, respectively. With all other parameters held constant, these plots illustrate how isolation compliance influences the transmission of the disease. The simulation results indicate that for $\delta = 0.01$ and $\delta = 0.001$ (Figure 12(a, b)), the

saddle-node bifurcation point shifts toward the threshold $R_0 = 1$ as the compliance parameter ε increases (i.e., compliance decreases), resulting in a reduced bifurcation gap $\Delta R = 1 - R_{Ci}$. This shift signifies enhanced epidemic controllability and a decline in the final number of infections, $I + I_T$, as shown in Figure 12(a, b) (i.e., Point $a > b > c$). This counterintuitive result suggests that under severely constrained isolation resources, high compliance alone may be insufficient to suppress the outbreak, due to nonlinear interactions between behavioral responses and capacity limitations. In contrast, when isolation resources are adequate ($\delta = 0.0001$), higher compliance (lower ε) consistently leads to a reduced infection burden (i.e., Point $c < b < a$ in Figure 12(c)), highlighting a synergistic control effect between resource availability and compliance, consistent with classical infectious disease theory.

4.3. Impact of isolation delays

Due to limited medical resources, infected individuals cannot always be isolated promptly. As a result, isolation is subject to a time delay. To account for this, we now present a model that incorporates the time delay in isolation [47, 48].

$$\begin{aligned}
\frac{\mathrm{d}S}{\mathrm{d}t} &= \Lambda - \lambda(t)S(t) - \mu S(t),\\
\frac{\mathrm{d}I_T}{\mathrm{d}t} &= \sigma\lambda(t)S(t) - \mu I_T(t) - \epsilon\theta I_T(t) - \frac{(1-\epsilon)\theta I_T(t-\tau)}{1+\delta I_T(t-\tau)},\\
\frac{\mathrm{d}I}{\mathrm{d}t} &= (1-\sigma)\lambda(t)S(t) + \epsilon\theta I_T(t) - (\mu+\gamma_I)I(t).
\end{aligned}$$

where $\lambda(t) = \mu\beta(\rho I_T(t-\tau) + I(t))/\Lambda$.

In this model, we introduce a new parameter τ to represent the time delay in isolation. We assume that there is a fixed time delay, τ, between the detection of an infected individual and their actual isolation. The values of $\tau = 1, 3$, and 7 days are selected to represent low, medium, and high isolation delays, respectively [47, 48]. Furthermore, it is assumed that this delay is the same for all infected individuals, neglecting potential variations in quarantine delays due to individual differences. Numerical simulations are employed to analyze the impact of isolation delay on disease transmission and control, as illustrated in Figure 13. We set $\delta = 0.0008$ and $\epsilon = 0.3$, and the remaining other parameters are shown in Table 1.

Figure 13(a, b) presents the simulation results for $\beta = 0.25$ and $R_0 = 1.1923$. In Figure 13(a), the blue curve represents the infection trajectory I when the isolation time delay $\tau = 3$, while the red curve illustrates the case without any isolation time delay. It is evident that the presence of a time delay in isolation leads to increased oscillation amplitudes, with higher peak values and delayed oscillatory behavior. This indicates that isolation time delays can amplify fluctuations in epidemic dynamics. Figure 13(b) compares the infection dynamics for $\tau = 1$, 3, and 7, showing that a shorter isolation time delay results in a reduced peak in the oscillations. This highlights the importance of prompt isolation in reducing the epidemic's severity.

Figure 13(c, d) corresponds to the simulation results when $\beta = 0.28$ and $R_0 = 1.3354$. In Figure 13(c), the blue curve represents the trajectory of I when the isolation time delay is $\tau = 3$, while the red curve corresponds to the case without an isolation delay. The presence of an isolation time delay leads to a higher infection peak, indicating an increase in the number of infections. However,

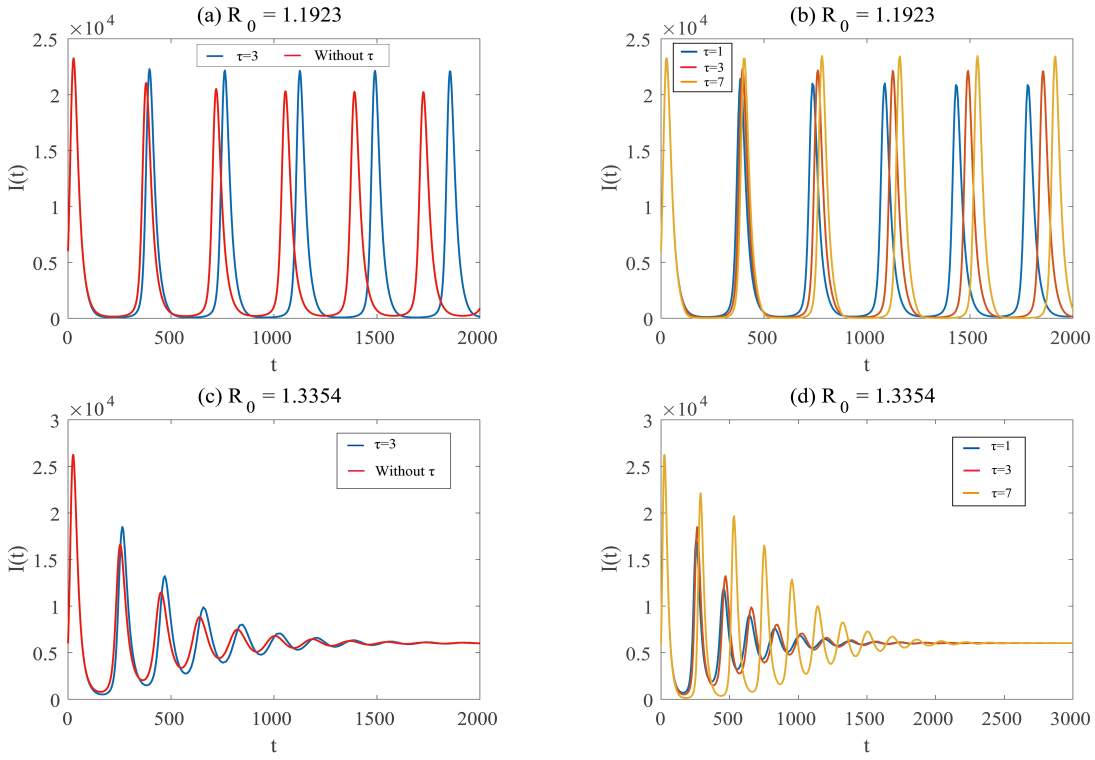

Figure 13. Effect of isolation time delay on the number of infections I. (a) and (c) Contrasts with and without time delay. (b) and (d) The effect of the size of the time delay, where $\tau = 1$, 3, and 7 represent low, medium, and high isolation delays, respectively.

the final number of infections remains unchanged. Figure 13(d) compares the infection trajectories for $\tau = 1$, 3, and 7. The results show that reducing the isolation delay significantly lowers the peak infection value, thereby decreasing the number of infections at the peak, while the final epidemic size remains the same. These findings emphasize that early isolation is essential for curbing the severity of epidemics and limiting their spread.

4.4. Timeliness of isolation

To explore how the timing of isolation resource deployment affects the effectiveness of epidemic control, we conducted numerical simulations to evaluate how increasing the isolation capacity at different stages of the epidemic affects the number of infected individuals. We performed numerical simulations to evaluate how augmenting the isolation capacity at different stages of the outbreak impacts the progression of infections. In particular, we investigated the temporal dynamics of infection numbers by adjusting isolation resource availability at various time intervals (e.g., Day 20 vs. Day 70) during the epidemic. This approach enables a quantitative assessment of the timeliness and effectiveness of isolation interventions, thereby providing insight into the optimal scheduling of resource allocation for mitigating disease transmission.

Figure 14 presents the simulation results, illustrating the temporal evolution of the number of infected individuals under two distinct intervention timings. We set $\delta = 0.01$, 0.002, 0.0005, and $\epsilon = 0.3$, and the remaining other parameters are shown in Table 1.

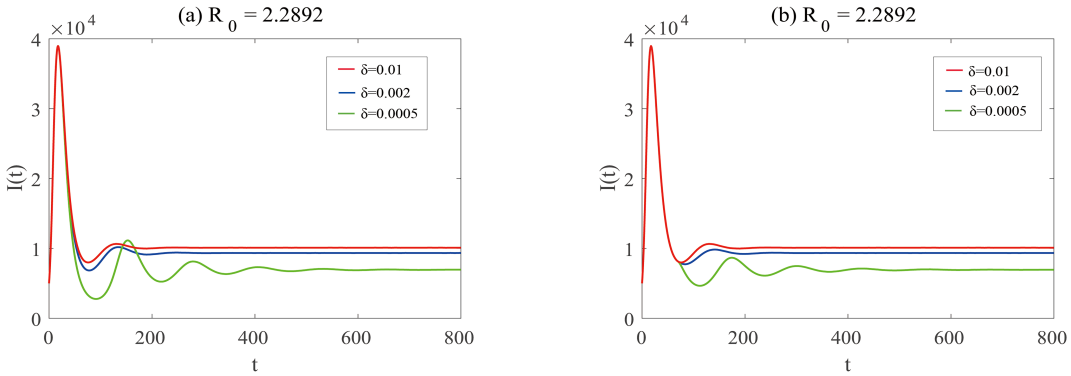

Figure 14. The timeliness of segregation, with (a) increasing the amount of segregated resources at 20 days and (b) increasing the amount of segregated resources at 70 days. The baseline case ($\delta = 0.01$, red curve) is used as the control group, and compared with two intervention scenarios: $\delta = 0.002$ (blue curve) and $\delta = 0.0005$ (green curve).

Figure 14 illustrates the moderating effect of the timeliness of isolation interventions on the dynamics of the epidemic's spread according to the numerical simulations. Figure 14 (a, b) depicts the impact of enhancing quarantine resources, corresponding to reductions in the quarantine resource parameter δ, on the evolution of size of the infected population when the intervention is implemented on Day 20 and Day 70. The baseline case ($\delta = 0.01$, red curve) serves as the control group and is compared with two intervention scenarios: $\delta = 0.002$ (blue curve) and $\delta = 0.0005$ (green curve).

In Figure 14(a), the increase in isolation resources markedly alters the infection dynamics. The number of infected individuals decreases significantly during the early stage of the epidemic, and the suppressive effect becomes more pronounced as δ decreases (green and blue curves). Notably, the peak

of the green curve exceeds that of the blue curve in the mid-stage of disease progression, resulting in a subpeak phenomenon. Ultimately, the system converges to a much lower endemic level, confirming the dual positive effects of early reinforcement of isolation, namely delaying the outbreak and reducing the final infection size.

As shown in Figure 14(b), increasing the isolation resources on Day 70 still results in a decrease in the final number of infections. However, compared with Figure 14(a), the intervention implemented at this later stage exhibits a substantially weaker suppressive effect during the early phase of the disease's spread. This comparison highlights the critical importance of timely enhancement of isolation capacity in effectively mitigating the spread of infection.

In summary, timely resource-based interventions are crucial for effective epidemic control. Early enhancement of isolation capacity significantly improves the suppression of the disease's spread. This underscores the need for governments to identify risks promptly, respond decisively, and prioritize the rapid deployment of isolation resources to achieve targeted and efficient outbreak mitigation.

5. Conclusion and discussion

In the early stages of EIDs, limited emergency preparedness often results in a shortage of isolation resources and inadequate compliance with isolation protocols. To explore the combined impact of these limitations on disease transmission and their implications for control strategies, we propose a mathematical model that incorporates saturated isolation rates. Through both theoretical analysis and numerical simulations, we examined how constrained isolation capacity and incomplete compliance influence the dynamics of the epidemic's spread.

From an analytical perspective, we establish the well-posedness of Model (2.3) (Theorem 3.1) and prove the stability of the DFE (Theorems 3.2 and 3.3). We further analyze the existence of EEs and provide a global threshold characterization of R_0. Specifically, when $0 < R_0 < R^*$, the DFE is globally asymptotically stable, indicating that the disease will eventually die out (Theorem 3.3). When $R_c < R_0 < 1$, a backward bifurcation may occur under certain conditions (Theorem 3.4). For $R_0 > 1$, the model exhibits uniform persistence, implying that the disease will persist in the population (Theorem 3.6). The emergence of phenomena such as backward bifurcation and uniform persistence suggests that limited resources can generate complex dynamics, complicating disease control. Our analysis provides a comprehensive theoretical framework for assessing the interplay between resource constraints and compliance.

Numerical simulations reveal a rich spectrum of dynamics, including forward, backward, Hopf, and saddle-node bifurcations. As the resource parameter δ increases (indicating a decrease in isolation capacity), the system undergoes a transition from forward to backward bifurcation (Figure 11). When isolation resources are sufficient, higher compliance leads to a smaller scale of infection (Figure 12(c)). However, when both isolation compliance and isolation resources vary simultaneously, insufficient resources may give rise to complex transmission patterns. Notably, under certain circumstances, a higher compliance level combined with low isolation resources may lead to increased infection risk and prevalence (Figure12(a, b)). The elucidation of this mechanism not only provides a theoretical foundation for the real-world phenomenon of high compliance yet ineffective control but also highlights the critical nonlinear interaction between behavior and resources. Additionally, reducing isolation delays significantly suppresses infection peaks and alleviates

healthcare burdens (Figure 13).

Overall, the numerical simulations comprehensively support and extend the theoretical analysis, and constitute a key component of this study by highlighting the intricate interplay of isolation capacity, compliance behavior, and temporal intervention factors.

Compared with previous studies [24,26,30,49], our integrated approach reveals distinctive insights. While Ahmad et al. and Gao et al. focused on individual factors, our concurrent analysis of resource saturation and behavioral compliance uncovers a novel paradox.

Moreover, the modeling framework proposed in this study is generalizable and can be extended to investigate the combined effects of other intervention factors, such as vaccination or limited testing resources. By adjusting the parameter settings, it can also be adapted to various scenarios, such as COVID-19, influenza, and other sudden outbreaks of infectious diseases. This demonstrates the broader applicability of our approach and its potential to inform public health decision-making in complex epidemic contexts.

Our analysis yields several key policy implications.

- Maintaining isolation capacity above critical thresholds is essential, even when $R_0 < 1$, to prevent backward bifurcation.
- Interventions should be implemented early—within 20 days of detecting the initial case—to maximize the effectiveness of reducing the infection burden and preventing recurrent outbreak waves.
- Public health strategies must synergistically enhance both isolation capacity and public compliance to mitigate the risk that high compliance, paradoxically, intensifies the outbreak's severity under resource constraints.

This study has several limitations that suggest promising directions for future research. First, the assumption of perfect case detection is idealized; incorporating testing inaccuracies would enhance realism. Second, the dynamic behavior for $R^* < R_0 < R_C$ requires further theoretical investigation. Third, extending the framework to account for asymptomatic transmission and demographic heterogeneity would broaden its applicability across diverse epidemiological contexts. Subsequent studies could also examine the coupled effects of parameters such as testing rates (σ) and reductions in infectiousness (ρ), and systematically evaluate differential impacts of isolation on symptomatic versus asymptomatic populations [50–52]. Finally, exploring the interactions between isolation and other interventions [53] would yield a more comprehensive understanding of coordinated outbreak control.

In summary, this research provides a comprehensive theoretical foundation for understanding the intricate interplay between behavioral compliance and resource allocation in epidemic control, offering actionable insights for designing public health strategies in resource-constrained settings.

Use of AI tools declaration

The authors declare they have not used artificial intelligence (AI) tools in the creation of this article.

Acknowledgments

This research is supported by the National Natural Science Foundation of China (No. 12271401, W2421101) and the Natural Science Foundation of Tianjin, China (No. 22JCYBJC00080). The authors extend their thanks to the handling editor and the referees for their valuable comments and suggestions, which significantly improved this paper.

Conflict of interest

The authors declare there is no conflict of interest. Shengqiang Liu is an editorial board member for *Mathematical Biosciences and Engineering* and was not involved in the editorial review or the decision to publish this article.

References

1. D. M. Morens, G. K. Folkers, A. S. Fauci, The challenge of emerging and re-emerging infectious diseases, *Nature*, **430** (2004), 242–249. https://doi.org/10.1038/nature02759
2. K. E. Jones, N. G. Patel, M. A. Levy, A. Storeygard, D. Balk, J. L. Gittleman et al., Global trends in emerging infectious diseases, *Nature*, **451** (2008), 990–993. https://doi.org/10.1038/nature06536
3. N. Wang, L. Qi, M. Bessane, M. Hao, Global Hopf bifurcation of a two-delay epidemic model with media coverage and asymptomatic infection, *J. Differ. Equations*, **369** (2023), 1–40. https://doi.org/10.1016/j.jde.2023.05.036
4. N. Wang, L. Qi, G. Cheng, Dynamical analysis for the impact of asymptomatic infective and infection delay on disease transmission, *Math. Comput. Simul.*, **200** (2022), 525–556. https://doi.org/10.1016/j.matcom.2022.04.029
5. P. P. Win, Z. Lin, M. Zhang, The final size and critical times of an SIVR epidemic model, *Adv. Contin. Discrete Models*, **2025** (2025), 31. https://doi.org/10.1186/s13662-025-03902-2
6. M. Jusup, P. Holme, K. Kanazawa, M. Takayasu, I. Romić, Z. Wang et al., Social physics, *Phys. Rep.*, **948** (2022), 1–148. https://doi.org/10.1016/j.physrep.2021.10.005
7. Y. Li, Y. Yao, M. Feng, J. Wang, L. Wang, Epidemic dynamics in homes and destinations under recurrent mobility patterns, *Chaos Solitons Fractals*, **195** (2025), 116273. https://doi.org/10.1016/j.chaos.2025.116273
8. W. Wu, Q. Zhang, H. Wang, S. Liu, Cholera dynamics driven by human behavior change via a degenerate reaction-diffusion model, *Z. Angew. Math. Phys.*, **76** (2025), 114. https://doi.org/10.1007/s00033-025-02495-w
9. R. J. Thorneloe, E. N. Clarke, M. A. Arden, Adherence to behaviours associated with the test, trace, and isolate system: an analysis using the theoretical domains framework, *BMC Public Health*, **22** (2022), 567. https://doi.org/10.1186/s12889-022-12815-8
10. C. N. Ngonghala, E. Iboi, S. Eikenberry, M. Scotch, C. R. MacIntyre, M. H. Bonds et al., Mathematical assessment of the impact of non-pharmaceutical interventions on curtailing the 2019 novel Coronavirus, *Math. Biosci.*, **325** (2020), 108364. https://doi.org/10.1016/j.mbs.2020.108364

11. T. Yu, D. Cao, S. Liu, Epidemic model with group mixing: Stability and optimal control based on limited vaccination resources, *Commun. Nonlinear Sci. Numer. Simul.*, **61** (2018), 54–70. https://doi.org/10.1016/j.cnsns.2018.01.011
12. H. Zhang, Z. Yang, K. A. Pawelek, S. Liu, Optimal control strategies for a two-group epidemic model with vaccination-resource constraints, *Appl. Math. Comput.*, **371** (2020), 124956. https://doi.org/10.1016/j.amc.2019.124956
13. Z. Liu, D. Qiu, S. Liu, A two-group epidemic model with heterogeneity in cognitive effects, *Math. Biosci. Eng.*, **22** (2025), 1109–1139. https://doi.org/10.3934/mbe.2025040
14. X. Pian, Y. Takeuchi, P. Yan, S. Liu, Paradox of vaccination in the context of avian influenza strain mutation, *Int. J. Biomath.*, (2025), 2550095. https://doi.org/10.1142/S1793524525500950
15. D. Barbisch, K. L. Koenig, F.-Y. Shih, Is there a case for quarantine? Perspectives from SARS to Ebola, *Disaster Med. Public Health Prep.*, **9** (2015), 547–553. https://doi.org/10.1017/dmp.2015.38
16. M. Martcheva, *An Introduction to Mathematical Epidemiology*, Springer, New York, 2015.
17. N. H. Nam, P. T. M. Tien, L. V. Truong, et al., Early centralized isolation strategy for all confirmed cases of COVID-19 remains a core intervention to disrupt the pandemic spreading significantly, *PLoS ONE*, **16** (2021), e0254012. https://doi.org/10.1371/journal.pone.0254012
18. Y. Niu, F. Xu, Deciphering the power of isolation in controlling COVID-19 outbreaks, *Lancet Glob. Health*, **8** (2020), e452–e453. https://doi.org/10.1016/S2214-109X(20)30085-1
19. H. Sjodin, A. Wilder-Smith, S. Osman, Z. Farooq, J. Rocklv, Only strict quarantine measures can curb the coronavirus disease (COVID-19) outbreak in Italy, 2020, *Eurosurveillance*, **25** (2020), 2000280. https://doi.org/10.2807/1560-7917.ES.2020.25.13.2000280
20. Z. Hu, S. Liu, H. Wang, Backward bifurcation of an epidemic model with standard incidence rate and treatment rate, *Nonlinear Anal. Real World Appl.*, **9** (2008), 2302–2312. https://doi.org/10.1016/j.nonrwa.2007.08.009
21. China Center for Disease Control and Prevention (China CCDC), National COVID-19 epidemic situation (September 2024) [Internet], Beijing: China CCDC; 2024 [cited 2025 Oct. 04]. Available from: https://www.chinacdc.cn/jksj/jksj01/202501/t20250117_303940.html
22. New Zealand Ministry of Health, National quarantine capability: Work programme and next steps [Internet], Wellington: Ministry of Health; 2024 [cited 2025 May 05]. Available from: https://www.health.govt.nz/system/files/2024-10/H2024045544.pdf.
23. X. Wang, Q. Li, X. Sun, et al., Effects of medical resource capacities and intensities of public mitigation measures on outcomes of COVID-19 outbreaks, *BMC Public Health*, **21** (2021), 1–11. https://doi.org/10.1186/s12889-021-10657-4
24. Z. Foroozanfar, M. Zamanian, R. Moradzadeh, F. Hajiabadi, J. Ahmadzadeh, Z. Hosseinkhani, Isolation compliance and associated factors among COVID-19 patients in north-west Iran: A cross-sectional study, *Int. J. Gen. Med.*, **13** (2020), 1697–1703. https://doi.org/10.2147/IJGM.S264227

25. J. E. Oeltmann, D. Vohra, H. H. Matulewicz, et al., Isolation and quarantine for coronavirus disease 2019 in the United States, 2020–2022, *Clin. Infect. Dis.*, **77** (2023), 212–219. https://doi.org/10.1093/cid/ciad163
26. S. Gao, P. Binod, C. W. Chukwu, T. Kwofie, S. Safdar, L. Newman et al., A mathematical model to assess the impact of testing and isolation compliance on the transmission of COVID-19, *Infect. Dis. Model.*, **8** (2023), 427–444. https://doi.org/10.1016/j.idm.2023.04.005
27. A. Steens, B. F. De Blasio, L. Veneti, A. Gimma, W. J. Edmunds, K. Van Zandvoort et al., Poor self-reported adherence to COVID-19-related quarantine/isolation requests, Norway, April to July 2020, *Eurosurveillance*, **25** (2020), 2001607. https://doi.org/10.2807/1560-7917.ES.2020.25.37.2001607
28. R. N. Shalan, R. Shireen, A. H. Lafta, Discrete an SIS model with immigrants and treatment, *J. Interdiscip. Math.*, **24** (2020), 1201–1206. https://doi.org/10.1080/09720502.2020.1814496
29. W. O. Kermack, A. G. McKendrick, A contribution to the mathematical theory of epidemics, *Proc. R. Soc. Lond. A*, **115** (1927), 700–721. https://doi.org/10.1098/rspa.1927.0118
30. I. Ahmad, H. Seno, An epidemic dynamics model with limited isolation capacity, *Theor. Biosci.*, **142** (2023), 259–273. https://doi.org/10.1007/s12064-023-00399-9
31. Z. Fu, H. Seno, SIRI+Q model with a limited capacity of isolation, *Theor. Biosci.*, **141** (2025), 1–24. https://doi.org/10.1007/s12064-025-00437-8
32. H. Zhao, L. Wang, S. M. Oliva, H. Zhu, Modeling and dynamics analysis of Zika transmission with limited medical resources, *Bull. Math. Biol.*, **82** (2020), 1–50. https://doi.org/10.1007/s11538-020-00776-1
33. J. Wang, S. Liu, B. Zheng, Y. Takeuchi, T. K. N. Do, Qualitative and bifurcation analysis using an SIR model with a saturated treatment function, *Math. Comput. Model.*, **55** (2012), 710–722. https://doi.org/10.1016/j.mcm.2011.08.045
34. V. Nenchev, Optimal quarantine control of an infectious outbreak, *Chaos Solitons Fractals*, **138** (2020), 110139. https://doi.org/10.1016/j.chaos.2020.110139
35. T. Zhou, W. Zhang, Q. Lu, Bifurcation analysis of an SIS epidemic model with saturated incidence rate and saturated treatment function, *Appl. Math. Comput.*, **226** (2014), 288–305. https://doi.org/10.1016/j.amc.2013.10.020
36. B. Buonomo, R. Della Marca, A. d'Onofrio, M. Groppi, A behavioural modelling approach to assess the impact of COVID-19 vaccine hesitancy, *J. Theor. Biol.*, **534** (2022), 110973. https://doi.org/10.1016/j.jtbi.2021.110973
37. World Health Organization, COVID-19 epidemiological update – 9 October 2024 [Internet], Geneva: WHO; 2024 [cited 2025 Oct. 04]. Available from: https://www.who.int/publications/m/item/covid-19-epidemiological-update-edition-172.
38. Tianjin Center for Disease Control and Prevention, Epidemic situation of notifiable infectious diseases in Tianjin in January 2022 [Internet], Tianjin: CDCTJ; 2022 [cited 2025 Oct. 04]. Available from: https://www.cdctj.com.cn/system/2022/02/17/030075597.shtml.
39. P. Van den Driessche, Reproduction numbers of infectious disease models, *Infect. Dis. Model.*, **2** (2017), 288–303. https://doi.org/10.1016/j.idm.2017.06.002

40. O. Diekmann, J. A. P. Heesterbeek, J. A. J. Metz, On the definition and the computation of the basic reproduction ratio R_0 in models for infectious diseases in heterogeneous populations, *J. Math. Biol.*, **28** (1990), 365–382. https://doi.org/10.1007/BF00178324

41. J. P. LaSalle, *The Stability of Dynamical Systems*, CBMS-NSF Regional Conference Series in Applied Mathematics, SIAM, 1976.

42. N. Wang, L. Yang, S. Liu, Stochastic dynamics of coral and macroalgae: Analyzing extinction and resilience in coral reef ecosystems, *Bull. Math. Biol.*, **87** (2025), 99. https://doi.org/10.1007/s11538-025-01479-1

43. X. Wang, A simple proof of Descartes's rule of signs, *Am. Math. Monthly*, **111** (2004), 525–526. https://doi.org/10.1080/00029890.2004.11920108

44. C. Castillo-Chavez, B. Song, Dynamical models of tuberculosis and their applications, *Math. Biosci. Eng.*, **1** (2004), 361–404. https://doi.org/10.3934/mbe.2004.1.361

45. C. Chen, Y. Xiao, Modeling saturated diagnosis and vaccination in reducing HIV/AIDS infection, *Abstr. Appl. Anal.*, **2014** (2014), 414383. https://doi.org/10.1155/2014/414383

46. Health Commission of Hubei Province, COVID-19 epidemic situation in Hubei Province on February 20, 2020 [Internet], Wuhan: Health Commission of Hubei Province; 2020 [cited 2025 May 05]. Available from: https://wjw.hubei.gov.cn/bmdt/ztzl/fkxxgzbdgrfyyq/xxfb/202002/t20200221_2144225.shtml.

47. H. Song, R. Wang, S. Liu, Z. Jin, D. He, Global stability and optimal control for a COVID-19 model with vaccination and isolation delays, *Results Phys.*, **42** (2022), 106011. https://doi.org/10.1016/j.rinp.2022.106011

48. M. A. Safi, A. B. Gumel, The effect of incidence functions on the dynamics of a quarantine/isolation model with time delay, *Nonlinear Anal. Real World Appl.*, **12** (2011), 215–235. https://doi.org/10.1016/j.nonrwa.2010.06.009

49. Z. Memon, S. Qureshi, B. R. Memon, Assessing the role of quarantine and isolation as control strategies for COVID-19 outbreak: a case study, *Chaos Solitons Fractals*, **144** (2021), 110655. https://doi.org/10.1016/j.chaos.2021.110655

50. M. Shen, Y. Xiao, G. Zhuang, Y. Li, L. Zhang, Mass testing—An underexplored strategy for COVID-19 control, *The Innovation*, **2** (2021), 100114. https://doi.org/10.1016/j.xinn.2021.100114

51. D. P. Oran, E. J. Topol, Prevalence of asymptomatic SARS-CoV-2 infection: a narrative review, *Ann. Intern. Med.*, **173** (2020), 362–367. https://doi.org/10.7326/M20-3012

52. M. A. Seibold, C. M. Moore, J. L. Everman, B. J. M. Williams, J. D. Nolin, A. Fairbanks-Mahnke et al., Risk factors for SARS-CoV-2 infection and transmission in households with children with asthma and allergy: A prospective surveillance study, *J. Allergy Clin. Immunol.*, **150** (2022), 302–311. https://doi.org/10.1016/j.jaci.2022.05.014

53. B. Nussbaumer-Streit, V. Mayr, A. I. Dobrescu, A. Chapman, E. Persad, I. Klerings et al., Quarantine alone or in combination with other public health measures to control COVID-19: a rapid review, *Cochrane Database Syst. Rev.*, (2020), CD013574. https://doi.org/10.1002/14651858.CD013574

Supplementary

Numerical simulation code

The numerical simulation source code referenced in the main text is provided to facilitate replication of our results. The archive file "MATLAB Code.zip" contains scripts for the model simulation, bifurcation analysis, and sensitivity analysis, implemented in MATLAB R2020b. Detailed comments are included within the code to explain the key steps.

Sensitivity analysis

Quantifying the parameter's sensitivity is crucial for understanding how uncertainties in the assumptions and estimates affect the dynamics of Model (2.1). In this section, we employ the partial rank correlation coefficient (PRCC) method to quantitatively assess the sensitivity of the parameters to the basic reproduction number $\bar{R}_0$.

We derive the basic reproduction number for Model (2.1) using the NGM method [39]. The model has a DFE $\bar{E}_0 = (\bar{S}_0, 0, 0, 0, 0)$, where $\bar{S}_0 = \Lambda/\mu$. Considering the infected compartments I_T and I, the matrices for new infection terms ($\bar{\mathcal{F}}$) and transition terms ($\bar{\mathcal{V}}$) are

$$\begin{pmatrix} \dfrac{\mathrm{d}I_T}{\mathrm{d}t} \\ \dfrac{\mathrm{d}I}{\mathrm{d}t} \end{pmatrix} = \bar{\mathcal{F}}(I_T, I) - \bar{\mathcal{V}}(I_T, I) = \begin{pmatrix} \dfrac{\sigma\beta(\rho I_T + I)S}{S + I_T + I + R} \\ \dfrac{(1-\sigma)\beta(\rho I_T + I)S}{S + I_T + I + R} \end{pmatrix} - \begin{pmatrix} (\mu + \mu_I + \epsilon\theta)I_T + \dfrac{(1-\epsilon)\theta I_T}{1 + \delta I_T} \\ (\mu + \mu_I + \gamma_I)I - \epsilon\theta I_T \end{pmatrix}.$$

Linearizing around $\bar{E}_0$ yields

$$\bar{F} = D\bar{\mathcal{F}}(I_T, I)\big|_{\bar{E}_0} = \begin{pmatrix} \sigma\rho\beta & \sigma\beta \\ (1-\sigma)\rho\beta & (1-\sigma)\beta \end{pmatrix}, \quad \bar{V} = D\bar{\mathcal{V}}(I_T, I)\big|_{\bar{E}_0} = \begin{pmatrix} \mu + \mu_I + \theta & 0 \\ -\epsilon\theta & \mu + \mu_I + \gamma_I \end{pmatrix}.$$

The NGM is given by $\bar{K} = \bar{F}\bar{V}^{-1}$. We now compute $\bar{V}^{-1}$ and $\bar{F}\bar{V}^{-1}$

$$\bar{V}^{-1} = \begin{pmatrix} \dfrac{1}{\mu + \mu_I + \theta} & 0 \\ \dfrac{\epsilon\theta}{(\mu + \mu_I + \theta)(\mu + \mu_I + \gamma_I)} & \dfrac{1}{\mu + \mu_I + \gamma_I} \end{pmatrix}, \quad \bar{F}\bar{V}^{-1} = \begin{pmatrix} \bar{Z} & \dfrac{\sigma\beta}{\mu + \mu_I + \gamma_I} \\ \bar{Z}_1 & \dfrac{(1-\sigma)\beta}{\mu + \mu_I + \gamma_I} \end{pmatrix}.$$

$$\bar{Z} = \frac{\sigma\rho\beta}{\mu + \mu_I + \theta} + \frac{\epsilon\theta\sigma\beta}{(\mu + \mu_I + \theta)(\mu + \mu_I + \gamma_I)}, \text{ and } \quad \bar{Z}_1 = \frac{(1-\sigma)\rho\beta}{\mu + \mu_I + \theta} + \frac{\epsilon\theta(1-\sigma)\beta}{(\mu + \mu_I + \theta)(\mu + \mu_I + \gamma_I)}.$$

The NGM is $\bar{K} = \bar{F}\bar{V}^{-1}$. The basic reproduction number $\bar{\mathcal{R}}_0$ is the spectral radius of $\bar{K}$, which is given by

$$\bar{\mathcal{R}}_0 = \frac{(1-\sigma)\beta}{\mu + \mu_I + \gamma_I} + \frac{\sigma\rho\beta}{\mu + \mu_I + \theta} + \frac{\epsilon\theta\sigma\beta}{(\mu + \mu_I + \theta)(\mu + \mu_I + \gamma_I)}.$$

We adopt the PRCC method to quantitatively illustrate the sensitivity of the parameters to the basic reproduction number $\bar{R}_0$. Here, $\bar{R}_0$ is selected as our response function, and the input parameters assumed are β, σ, μ, γ_I, ρ, ϵ, θ, and μ_I. We take the parameter values from Table 1 as the baseline. The

range for each parameters is set to approximately 20% above and below the baseline value. Figure 15 presents the PRCC results, where the magnitude indicates the strength of the influence and the sign indicates the direction (positive or negative) of the correlation.

Sensitivity analysis based on PRCC identifies the parameters exerting a significant influence on the basic reproduction number $\bar{R}_0$ (Figure 15). The transmission rate β demonstrates the strongest positive correlation. The proportion of noncompliant individuals ϵ and the infectiousness reduction factor ρ also exhibit positive correlations. Conversely, the recovery rate γ_I, the testing proportion σ, the test result waiting rate θ, and the natural death rate μ are all negatively correlated. Most critically, the disease-induced death rate μ_I shows a negligible effect, thereby providing a solid justification for its exclusion ($\mu_I = 0$) in the simplified model analyzed in the main text.

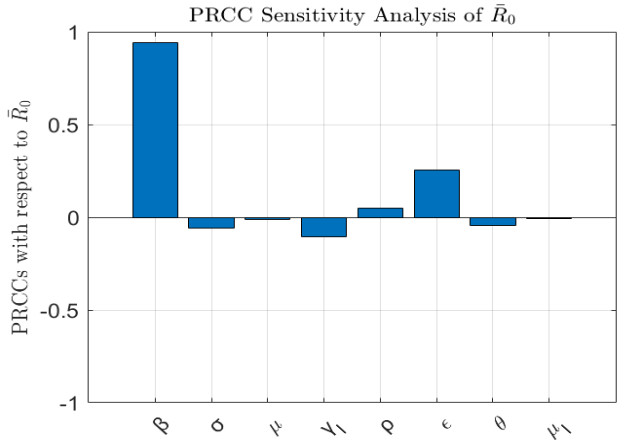

Figure 15. PRCC sensitivity analysis of the parameters for $\bar{R}_0$.